Investigating the role of dust in ice nucleation within clouds and further effects on the regional weather system over East Asia

Part II: modification of the weather system

Lin Su[1], and Jimmy C.H. Fung[2, 3]

[1] School of Science, Hong Kong University of Science and Technology, Hong Kong, China

[2] Division of Environment, Hong Kong University of Science and Technology, Hong Kong, China

[3] Department of Mathematics, Hong Kong University of Science and Technology, Hong Kong, China

Correspondence to: Lin Su (lsu@connect.ust.hk)

Keywords: East Asian dust; radiative forcing; clouds; precipitation; regional modeling

Highlights:

The semi-direct and indirect effects of dust are more pronounced than the direct effect on the regional weather system.

The semi-direct and indirect effects of dust result in an increase in mid- to high clouds, and a reduction in low clouds.

The total precipitation is reduced over most of China, but increased over South China by up to 20% or more.

Abstract. An updated version of the Weather Research and Forecast model coupled with Chemistry (WRF-Chem) was applied to quantify and discuss the full effects of dust on the meteorological field over East Asia during March and April 2012. The performances of the model in simulating the short-wave and long-wave radiation, surface temperature, and precipitation over East Asia are improved by incorporating the effects of dust in the simulations. The radiative forcing induced by the dust-enhanced cloud radiative effect is over one order of magnitude larger than that induced by the direct effect of dust. The semi-direct and indirect effects of dust result in a substantial increase in mid- to high clouds, and a significant reduction in low clouds, leading to a decrease of near-surface temperature and an increase of temperature at the mid- to upper troposphere over East Asia. The spatial redistribution of atmospheric water vapor and modification of the vertical temperature profile over East Asia lead to an inhibition of atmospheric instability over most land areas, but an enhancement of atmospheric instability over South China and the ocean, resulting in a significant inhibition of convective precipitation in areas from central to East China, and a substantial enhancement of convective precipitation over South China. Meanwhile, non-convective precipitation is also reduced significantly over East Asia, as cloud droplets are hindered from growing large enough to form rain droplets, due to the semi-direct and indirect effects of dust. The total precipitation can be reduced or increased by up to 20% or more.

1 Introduction

Dust is recognized as an "essential climate variable" because it is a major component of atmospheric aerosols and has significant impacts on the weather and climate system (Solomon, 2007). East Asian dust is an important contributor to global dust emissions (Ginoux et al., 2001), and thus play a significant role in affecting the regional weather system through direct effect, semi-direct and indirect effects.

Dust particles affect the radiation budget directly by absorbing, reflecting and scattering short-wave and long-wave radiation (Satheesh et al., 2006;Seinfeld et al., 2004;Lacis, 1995). The cloud radiative effect induced by dust is referred to as the semi-direct effect of dust. Dust particles within clouds can absorb radiation and heat up the surrounding environment, leading to faster evaporation rate of cloud droplets and thus a reduction of cloud cover. The indirect effects of dust are related to dust–cloud–interaction. (Hansen et al., 1997;Perlwitz and Miller, 2010). Dust particles are recognized as effective ice nuclei (IN) and considered to play an important role in cold cloud processes (Broadley et al., 2012;Connolly et al., 2009;Sassen, 2002), leading to the variation of the ice water content in mixed-phase and ice clouds, which further affects the formation and development of clouds, as well as precipitations (Sassen et al., 2003;Targino et al., 2006;Teller and Levin, 2006;Lohmann and Feichter, 2005).

In light of the significance of dust for the weather and climate system, assessing the effects of dust has become increasingly important. On one hand, the direct (Mallet et al., 2009;Nabat et al., 2015a;Ge et al., 2010;Hartmann et al., 2013;Huang et al., 2009;Bi et al., 2013;Liu et al., 2011a;Liu et al., 2011b;Palacios et al., 2015;Huang, 2017) and semi-direct (Tesfaye et al., 2015;Nabat et al., 2015b;Seigel et al., 2013) effects of dust has being extensively studied worldwide by applying numerical methods. On the other hand, various ice nucleation parameterizations have been implemented into global models to estimate the importance of dust in atmospheric ice nucleation (Lohmann and Diehl, 2006;Karydis et al., 2011;Hoose et al., 2008;Zhang et al., 2014), revealing that the effect of dust as IN should not be neglected in numerical models, especially in the simulations over arid regions during strong wind events (DeMott et al., 2003;Koehler et al., 2010;DeMott et al., 2015;Lohmann and Diehl, 2006;Atkinson et al., 2013). Unfortunately, , only limited work has been carried out to investigate the indirect effects of dust on the regional weather system, especially over East Asia, which is one of the major contributors to the global dust emission in the world (Ginoux et al., 2001).

59   This series of study aimed to investigate the role of East Asian dust in affecting the regional weather system. In the

60   first part of the study, The Goddard Chemistry Aerosol Radiation and Transport (GOCART) model has been coupled

61   with the aerosol-aware Thompson-Eidhammer microphysics scheme (Thompson and Eidhammer, 2014), enabling the

62   model to estimate the indirect effect of dust along with the direct and semi-direct effects, which improved the

63   simulation of the ice nucleation process involving dust particles (Su and Fung, 2017). In this work, by applying an

64   updated version of WRF-Chem, we aim to investigate the full effects of dust, including direct, semi-direct, and indirect

65   effects, on the regional weather system over East Asia during a dust-intensive period. This is the first study to

66   document the full effects of dust during a typical dust-intensive period over East Asia by applying an online-coupled

67   regional numerical model.

68   The remainder of the manuscript is organized as follows. The model configurations is described in Section 2, followed

69   by the model validation in Section 3. The results along with the discussion will be presented in section 4, followed by

70   the concluding remarks in Section 5.

71

72   **2 Model configurations**

73   The simulations were performed using an updated version of WRF-Chem based on version 3.8.1 (Grell et al., 2016).

74   The GOCART-Thompson, which is the coupling of the GOCART aerosol model and the aerosol-aware Thompson-

75   Eidhammer microphysics scheme, has been implemented in the updated WRF-Chem, to evaluate the indirect effect

76   of dust on the atmospheric ice nucleation process by serving as IN. In the GOCART-Thompson microphysics scheme,

77   the deposition nucleation is determined by the parameterization of Phillips et al. (Phillips et al., 2008), and the freezing

78   of deliquesced aerosols using the hygroscopic aerosol concentration is parameterized following Koop et al. (Koop et

79   al., 2000), with the background aerosol concentration set to be 1/L. In addition, the condensation and immersion

80   freezing is parameterized by the DeMott2015 ice nucleation scheme, and two factors of the DeMott2015 scheme were

81   tuned through sensitivity experiments in the first part of this study. c_f is a calibration factor in the DeMott2015 ice

82   nucleation parameterization scheme, which was used for the nucleation of the heterogeneous nucleation of ice crystals

83   by dust particles in the GOCART-Thompson scheme, and it ranges from 1 to 6. According to the results of the

84   sensitivity experiments in Part I, the calibration factor c_f was set to be 4 for the simulations in this study. Furthermore,

85   it was also demonstrated that the ice water content was still underestimated by using the GOCART-Thompson scheme.

86   To improve the simulation of the ice nucleation by dust particles, the threshold relative humidity with respect to ice

87   (RH_i) was lowered from 105% to 100% in the ice nucleation parameterization, to allow the heterogeneous nucleation

88   of ice crystals by dust particles to occur at a lower RH_i (Su and Fung, 2017). Therefore, a threshold RH_i of 100% was

89   for the simulations run with dust emissions in this study.

90   Four numerical simulations were carried out to evaluate the separate effects of dust over East Asia. The configurations

91   for the four simulations are summarized in Table 1. The first simulation was termed NO-DUST/NO-CLOUD, and

92   was conducted without dust, with both the aerosol radiative feedback and cloud radiative feedback turned off. The

93   second simulation, NO-DUST/CLOUD, was also conducted without dust, with the aerosol radiative feedback turned

94   off, but the cloud radiative feedback turned on to estimate the intrinsic radiative effect of cloud. The third simulation,

95   DUST/NO-CLOUD, was conducted with the presence of dust, with the aerosol radiative feedback turned on, while

96   the cloud radiative feedback still turned off. The difference between NO-DUST/NO-CLOUD and DUST/NO-CLOUD

97   therefore represented the direct effect of dust on the radiation budget and other meteorological parameters. The last

98   simulation, DUST/CLOUD, was conducted with the presence of dust, and with both aerosol radiative feedback and

99   cloud radiative feedback turned on, to estimate the full effect of dust on the meteorological field over East Asia.

100   The important physical and chemical parameterization schemes applied for the four simulations are as follows. The

101   GOCART aerosol model was applied to simulate the aerosol processes (Ginoux et al., 2001;Ginoux et al., 2004). For

102   the dust emission simulation in DUST/NO-CLOUD and DUST/CLOUD, the Shao dust emission scheme (Shao,

103   2004;Shao et al., 2011) was applied, which had been demonstrated to closely reproduced the dust emissions over East

104   Asia (Su and Fung, 2015). Note that no aerosol emissions were considered in the simulations other than dust. The

105   Mellor–Yamada–Janjic (MYJ) turbulent kinetic energy scheme was used for the planetary boundary layer

106   parameterization (Janjić, 2002, 1994); the moisture convective processes were parameterized by the Grell–Freitas

107   scheme (Grell and Freitas, 2014); the short-wave (SW) and long-wave (LW) radiation budgets were calculated by the

108   Rapid Radiative Transfer Model for General Circulation (RRTMG) SW and LW radiation schemes (Mlawer et al.,

109   1997;Iacono et al., 2008); gravitational settling and surface deposition were combined for aerosol dry deposition

110   (Wesely, 1989); a simple washout method was used for the below-cloud wet deposition of aerosols; and the aerosol

111   optical properties were calculated based on the volume-averaging method. The newly-implemented wet scavenging

112   scheme described in Part I of this study was used for the in-cloud wet scavenging of dust particles caused by the

113   microphysical processes. As no dust was simulated in NO-DUST/NO-CLOUD and NO-DUST/CLOUD, these two

114   simulations did not included a dust emission scheme, aerosol dry and wet deposition schemes, and aerosol optical

115   schemes. Note that in the two NO-CLOUD simulations, a default IN concentration of 1 per Liter is used for the

116   heterogeneous ice nucleation process.

117   As described in the first part of this manuscript, two nested domains were used for all four simulations, the outer

118   domain had a horizontal resolution of 27 km, covering the entire East Asia region, and the inner domain had a

119   horizontal resolution of 9 km, covering the entire central to East China. Both domains have 40 layers, with the top

120   layer at 50 hPa. The simulation period was March 9 to April 30, 2012, with the first eight days as "spin-up" time. Only

121   the results from March 17 to April 30, 2012 were used for further analysis. Final reanalysis data provided by the

122   United States National Centre of Environmental Prediction, with a horizontal resolution of 1°, were used for generating

123   the initial and boundary conditions for the meteorological field. The simulations were re-initialized every 4 days, with

124   the aerosol field being recycled, i.e., the output of the aerosol field from the previous 4-day run was used as the initial

125   aerosol state for the next 4-day run.

126

127   **3 Model validation**

128   The simulation for dust emission was validated in Part I of this study, and the model was demonstrated to closely

129   reproduce dust emissions over East Asia during the investigated period by comparison with comprehensive

130   observational data. As this study focused on the modification of the meteorological field by the effects of dust over

131   East Asia, the capability of the model in simulating the meteorological field itself over this region requires further

132   validation.

133   The China meteorological forcing dataset (Yang et al., 2010;Chen et al., 2011) was used to assess the performance of

134   the model in reproducing the spatial distribution of the meteorological field over China. The dataset was developed

135   by the hydrometeorological research group at the Institute of Tibetan Plateau Research, Chinese Academy of Science,

136   by merging the Princeton meteorological forcing data (Sheffield et al., 2006), the Global Energy and Water Cycle

137   Experiment–Surface Radiation Budget (GEWEX-SRB) forcing data (Pinker and Laszlo, 1992), and the Global Land

138   Data Assimilation System forcing dataset (Rodell et al., 2004). The dataset contains gridded observations of the near-

139   surface temperature, precipitation rate, surface downward SW and LW radiation across China, with a spatial resolution

140   of 0.25°, dating from 1996.

141   Note that only simulation results from NO-DUST/CLOUD and DUST/CLOUD are shown, as they represent the

142   intrinsic meteorological field and the meteorological field modified by the effects of dust, respectively. For March,

143   the comparison is restricted to the observational data from March 17 to March 31, 2012, to ensure temporal overlay

144   with the corresponding simulation period. No observational data over the ocean were available, so the simulated results

145   over the ocean are also omitted to simplify the comparison.

146   The spatial distributions for the monthly average observational downward surface SW radiation for March and April

147   2012 are shown in Figure 1a and b. Overall, the SW radiation was stronger in April than in March. The SW radiation

148   was significantly higher over the West and Northwest China, due to the higher elevation of terrain over these regions,

149   and lower over East and South China, due to the lower elevation and greater cloud coverage over those regions. The

150   model closely reproduced the spatial distributions of the SW radiation in both months and accurately captured the

151   trend from March to April in the simulation results from both NO-DUST/CLOUD and DUST/CLOUD, despite a

152   certain overestimation, especially over coastal areas of East and South China. This overestimation was likely due to

153   the underestimation of clouds by the model over these areas. Compared with inland areas, cloud coverage is always

154   greater over the coastal areas of East and South China due to the abundant water vapor. Therefore, the SW radiation

155   budget over coastal areas was more sensitive to the underestimation of clouds by the model. Nevertheless, an

156   improvement in the simulation of the SW radiation budget over East Asia can be seen in the results from

157   DUST/CLOUD compared with those from NO-DUST/CLOUD. Specifically, the SW radiation produced in

158   DUST/CLOUD (Figure 1e and f) was substantially lower than that produced in NO-DUST/CLOUD (Figure 1c and d)

159   over China, especially at the dust sources and surrounding areas over the north and northwest of the country, which is

160   clearly more consistent with the observations.

161   For downward surface LW radiation, two high-value areas can be observed (Figure 2a and b). One is over Northwest

162   China, where the Taklimakan Desert is located. The strong downward LW radiation over this region was likely due

163   to the abundance of dust particles in the local atmosphere. The other area of strong LW radiation was located over

164   South China, which is warmer and contains more atmospheric water vapor. Water vapor is a potent greenhouse gas,

165   which efficiently absorbs LW radiation emitted by the Earth and heat the surrounding area, and thus increases the

166   emission of LW radiation downward (and upward) by the heated atmosphere. The model accurately simulated the

167   spatial distributions of the LW radiation over this region for both March and April in both NO-DUST/CLOUD (Figure

168   2c and d) and DUST/CLOUD (Figure 2e and f), and indeed closely captured the spatial pattern of the LW radiation

169   over China. The LW radiation over the Gobi Desert produced by DUST/CLOUD (Figure 2e and f) is slightly higher

170 than that produced by NO-DUST/CLOUD, indicating that the model reproduced the LW radiation budget more

171 accurately upon taking the effects of dust into account.

172 Similarly to the spatial distributions for the LW radiation, higher near-surface temperatures were observed over

173 Northwest China, which is a dry, arid area, and South China, which is closer to the equator (Figure 3a and b). The

174 spatial distributions of the near-surface temperature over this region were well reproduced by the model for both

175 March and April in both NO-DUST/CLOUD (Figure 3c and d) and DUST/CLOUD (Figure 3e and f). The model

176 accurately captured the spatial pattern of the surface temperature, and the two simulations did not show remarkable

177 difference in their results.

178 During the simulation period, the precipitation increased from North to South China in both months, and increased

179 from March to April over the entire region (Figure 4a and b). The spatial patterns of precipitation in March and April

180 were mostly reproduced by the model in both NO-DUST/CLOUD (Figure 4c and d) and DUST/CLOUD (Figure 4e

181 and f), but the model underestimated the precipitation in March in both simulations, especially over central and North

182 China. In April, the observed precipitation center was located over South China. Apart from underestimating the

183 precipitation over Central and North China, the NO-DUST/CLOUD simulation predicted the precipitation center to

184 be located in an area to the north of the observed center (Figure 4d), and it also underestimated the precipitation over

185 South China. In contrast, in the results of DUST/CLOUD (Figure 4f), the precipitation band from Hunan to the north

186 of south China was markedly weaker, while the precipitation over South China was enhanced, which was clearly much

187 more consistent with the observations.

188 The foregoing comparison of the simulation results with the observational data demonstrated that the model reasonably

189 reproduced the meteorological field over East Asia. Moreover, the meteorological field was produced more accurately

190 when the effects of dust were considered in the simulations, which consequently allows the dust-induced modification

191 of the meteorological field to be investigated.

192

193 **4 Results and discussion**

194 **4.1 Radiative effect**

195 The radiative effect of dust particles is demonstrated by dust-induced SW, LW, and net radiative forcing at the top of

196 the atmosphere (TOA), at the bottom of the atmosphere (BOT), and within the atmosphere (ATM) in this study.

197 The spatial distributions for the mean radiative forcing induced by dust at the top of the atmosphere, at the bottom of

198   the atmosphere, and within the atmosphere over East Asia during the simulation period are shown in Figures 5 and 6.

199   Note that all of the spatial distributions for radiative forcing shown in the two figures are the temporal mean over the

200   entire simulation period. The SW radiative forcing was calculated as follows.

$$SW_{TOA} = SWDOWN_{TOA} - SWUP_{TOA} \tag{1}$$

$$SW_{BOT} = SWDOWN_{BOT} - SWUP_{BOT} \tag{2}$$

$$SW_{ATM} = SW_{TOA} + SW_{BOT} \tag{3}$$

204   where SW_{TOA} is the SW radiative forcing at the top of the atmosphere, and SW_{BOT} is the SW radiative forcing at the

205   bottom of the atmosphere, both with positive values representing downwelling radiation; SW_{ATM} is the radiative

206   forcing within the atmosphere, which is the sum of SW_{TOA} and SW_{BOT}, with positive values representing a net

207   warming effect within the atmosphere; $SWDOWN_{TOA}$ and $SWUP_{TOA}$ are the downwelling and upwelling SW

208   radiation at the top of the atmosphere, respectively; $SWUP_{BOT}$ and $SWDOWN_{BOT}$ are the upwelling and downwelling

209   SW radiation at the bottom of the atmosphere, respectively.

210   The LW radiative forcing was calculated as follows.

$$LW_{TOA} = -LWUP_{TOA} \tag{4}$$

$$LW_{BOT} = LWDOWN_{BOT} - LWUP_{BOT} \tag{5}$$

$$LW_{ATM} = LW_{TOA} + LW_{BOT} \tag{6}$$

214   Where LW_{TOA} is the LW radiative forcing at the top of the atmosphere, and LW_{BOT} is the LW radiative forcing at the

215   bottom of the atmosphere, both with positive values representing downwelling radiation; LW_{ATM} is the radiative

216   forcing within the atmosphere, which is the sum of LW_{TOA} and LW_{BOT}, with positive values representing warming

217   effect within the atmosphere; $LWUP_{TOA}$ is the upwelling LW radiation at the top of the atmosphere; $LWUP_{BOT}$ and

218    $LWDOWN_{BOT}$ are the upwelling and downwelling LW radiation at the bottom of the atmosphere.

219   The net radiative forcing is the sum of SW and LW radiative forcing.

$$Ra_{TOA} = SW_{TOA} + LW_{TOA} \tag{7}$$

$$Ra_{BOT} = SW_{BOT} + LW_{BOT} \tag{8}$$

$$Ra_{ATM} = SW_{ATM} + LW_{ATM} \tag{9}$$

223

4.1.1 Clear-sky radiative forcing

225   The direct radiative forcing induced by dust shown in Figure 5 is also referred to as clear-sky radiative forcing, and is

226 due to the reflection, absorption and emission of radiation by dust particles suspended in the atmosphere.

227 The clear-sky downwelling SW radiative forcing at the top of the atmosphere is slightly negative over most of East

228 Asia (Figure 5a), indicating that the upwelling SW radiation at the top of the atmosphere increases due to the reflection

229 and scattering of SW radiation by dust particles. The clear-sky SW radiative forcing at the bottom of the atmosphere

230 is negative over most of East Asia (Figure 5g), especially over dust source regions, which suggests that the

231 downwelling SW radiation is significantly reduced through the absorption by dust particles suspended in the

232 atmosphere, leading to a significant net warming effect within the atmosphere (Figure 5d). Averaged over the entire

233 simulation domain, the SW radiative forcing over East Asia is -1.22 W/m^2 at the top of the atmosphere, -2.44 W/m^2

234 at the bottom of the atmosphere, and 1.23 W/m^2 within the atmosphere, accounting for 0.37%, 0.97%, and 1.58% of

235 the total clear-sky radiation budget in these three zones, respectively, as shown in Table 2.

236 In Figure 5b, the clear-sky downwelling LW radiation at the top of the atmosphere is slightly increased over dust

237 source regions and downwind areas, due to the absorption of LW radiation by the thick dust layer with large fraction

238 of coarse particles in the atmosphere. In comparison, it is slightly reduced over other areas of East Asia, indicating an

239 increase of the upwelling LW radiation, which might be attributable to the greater emission of LW radiation by the

240 dust layer, which in turn is due to the heating of the atmosphere caused by the absorption of SW radiation by dust

241 particles (Figure 5d). The clear-sky downwelling LW radiation forcing is reduced at the bottom of the atmosphere

242 (Figure 5h), which is attributed to the Earth's surface being cooler as it receives less solar radiation (Figure 5g).

243 Combining the LW radiative forcing at the top of the atmosphere and at the bottom of the atmosphere, there is a net

244 negative LW radiative forcing within the atmosphere (Figure 5e). Overall, the mean LW radiative forcing averaged

245 over the entire East Asia is relatively slight, being -0.02 W/m^2 at the top of the atmosphere, 1.09 W/m^2 at the bottom

246 of the atmosphere, and -1.07 W/m^2 within the atmosphere, accounting for 0.01%, 1.18%, and 0.63% of the total clear-

247 sky radiation budget in those three zones, respectively.

248 Combining the SW and LW radiative forcing, the net downwelling clear-sky radiation at the top of the atmosphere is

249 reduced over most of East Asia (Figure 5c). The downwelling clear-sky net radiation at the bottom of the atmosphere

250 is reduced over most part of East Asia, especially over dust source regions and downstream areas (Figure 5i), leading

251 to a net warming effect within the atmosphere (Figure 5f), which is slightly smaller than the warming caused by SW

252 radiative forcing (Figure 5d). The net radiative forcing is -1.20 W/m^2 at the top of the atmosphere, -1.36 W/m^2 at the

253 bottom of the atmosphere, and 0.15 W/m^2 within the atmosphere, accounting for 1.78%, 0.85%, and 0.16% of the total

254   clear-sky radiation budget in those three zones.

255

256   **4.1.2 All-sky radiative forcing**

257   The all-sky radiative forcing induced by dust shown in Figure 6 is the total radiative forcing, including the radiative

258   forcing directly induced by dust displayed in Figure 5, and that induced by the cloud radiative effect enhanced by dust.

259   In Figure 6a, the all-sky downwelling SW radiation at the top of the atmosphere is markedly reduced over most of

260   China compared with the clear-sky case, due to greater reflection from dust and enhanced cloud cover induced by dust

261   over the continent. However, it is increased over the southern part of northwest Pacific, indicating less SW radiation

262   is reflected back into space due to the cloud radiative effect, which implies less cloud cover induced by dust over this

263   area. Compared with the clear-sky case, the all-sky upwelling SW radiation at the bottom of the atmosphere in Figure

264   6g is increased significantly over the continent, as more solar radiation is blocked due to the enhanced cloud cover

265   induced by dust; however, the downwelling all-sky SW radiation at the bottom of the atmosphere is reduced over most

266   of the West Pacific, indicating that more solar radiation that reaches the Earth's surface due to the cloud radiative

267   effect, which also implies less cloud cover over this area. The cloud radiative effect strengthens the warming within

268   the atmosphere over land in the all-sky case compared with the clear-sky case, while there is a slight cooling over the

269   ocean in the all-sky case, as shown in Figure 6d, in contrast to the slight warming in the clear-sky case. Averaged over

270   the entire simulation domain, the mean SW radiative forcing is -7.81 W/m^2 at the top of the atmosphere, and -7.87

271   W/m^2 at the bottom of the atmosphere (Table 2), accounting for 2.62% and 3.60% of the total all-sky radiation budget

272   in those two zones, respectively. Within the atmosphere, the positive SW radiative forcing over land and negative SW

273   radiative forcing over the ocean balance each other out.

274   Compared with the clear-sky case, the all-sky downwelling LW radiation at the top of the atmosphere is significantly

275   increased over almost the whole of East Asia (Figure 6b), indicating much less upwelling LW radiation at the top of

276   the atmosphere. The increase of downwelling all-sky LW radiation at the bottom of the atmosphere over land in Figure

277   6h is due to the greater emission of LW radiation by the warmer atmosphere, and the larger radiative forcing than that

278   in the clear-sky case implies that the cloud cover is significantly increased over land due to dust. Conversely, there is

279   no warming effect at the surface of the ocean, and the reduction in downwelling LW radiation over the ocean implies

280   less cloud cover over the ocean. The combination of the direct radiative effect of dust and the cloud radiative effect

281   enhanced by dust causes an overall increase of LW radiation within the atmosphere, leading to a warming effect,

282   which is more pronounced over the ocean, as shown in Figure 6e. The mean all-sky LW radiative forcing over the

283   entire simulation domain is 9.52 W/m^2 at the top of the atmosphere, accounting for 3.79% of the total all-sky LW

284   radiation budget in that zone. The increase of the all-sky LW radiation at the bottom of the at atmosphere over land

285   and its reduction over the ocean almost cancel each other out, leaving a mean all-sky LW radiation over the entire

286   simulation domain of 0.25W/m^2, accounting for 0.34% of the total LW radiation budget at the bottom of the

287   atmosphere. The mean all-sky LW radiative forcing within the atmosphere over the simulation domain is 9.26 W/m^2,

288   accounting for 5.25% of the total all-sky LW radiation budget within the atmosphere.

289   Summing the SW and LW radiative forcing, the net downwelling all-sky radiation at the top of the atmosphere is

290   reduced to the north of Central China, Korea, and Japan, and increased significantly over most of the ocean (Figure

291   6c). By contrast, the net downwelling all-sky net radiation at the bottom of the atmosphere is reduced significantly

292   over the same land areas, and increased over most of the ocean (Figure 6i). Radiative forcing results in pronounced

293   warming within the atmosphere over East Asia as a whole (Figure 6f). Averaged over the simulation domain, the net

294   all-sky radiative forcing is 1.70 W/m^2, -7.62 W/m^2, and 9.33 W/m^2 at the top of the atmosphere, at the bottom of the

295   atmosphere, and within the atmosphere, accounting for 3.61%, 5.28%, and 9.61% of the total net radiation budget in

296   those three zones, respectively.

297   In summary, the direct radiative effect of dust combined with the cloud radiative effect enhanced by dust causes a net

298   loss of radiation at the Earth's surface, but a net gain of radiation within the atmosphere, leading to a cooling at the

299   surface and lower troposphere, and a warming in mid- to upper troposphere. The radiative forcing caused by the dust-

300   enhanced cloud radiative effect is much greater than that caused by the direct radiative effect of dust, especially for

301   LW radiative forcing, which is highly affected by cloud cover. The LW radiative forcing caused by the dust-enhanced

302   cloud radiative effect is one order stronger than that cased by the direct radiative effect of dust at the top of the

303   atmosphere and within the atmosphere. The spatial distribution of radiative forcing further implies a shift of the spatial

304   distribution of cloud cover, such that the cloud cover is likely increased over land, but reduced over the ocean due to

305   the presence of dust, indicating a re-distribution of atmospheric water vapor over East Asia. The shift of the vertical

306   distribution of the radiation budget, the re-distribution of atmospheric water vapor, and the modification of

307   atmospheric stability resulting from those two processes will be discussed in more detail in later sections.

308

309   **4.2 Atmospheric water vapor**

4.2.1 Spatial distribution

The Semi-direct and indirect effects of dust particles lead to a modification of cloud format and cloud lifetime, and a re-distribution of atmospheric water vapor. The spatial distributions of the simulated atmospheric water vapor path, ice water path, and cloud water path from NO-DUST/CLOUD and DUST/CLOUD, as well as the difference (DUST/CLOUD − NO-DUST/CLOUD) between the two simulations, are presented in Figure 7. The atmospheric water vapor path, ice water path, and cloud water path are the column sums of water vapor, ice water vapor, and cloud water vapor in the atmosphere per unit area. Note that the difference between NO-DUST/CLOUD and DUST/CLOUD is entirely due to the combined effects of dust, i.e., the direct effect of dust, the cloud radiative effect enhanced by dust, and the microphysical effect of dust serving as IN in the atmosphere. The spatial distributions shown in Figure 7 are the mean atmospheric water vapor path, ice water path, and cloud water path averaged over the whole simulation period.

Figure 7a and b show the spatial distributions of precipitable water vapor in the atmosphere, which is equal to the total volume of the atmospheric water path in the atmospheric column, over East Asia produced from NO-DUST/CLOUD and DUST/CLOUD. The results from the two simulations are similar, with the same spatial pattern. The differences between the two are shown in Figure 7c, in which the precipitable water vapor is slightly reduced by less than 1 mm over most of East Asia, except for the dust source regions, over where the precipitable water vapor in the atmosphere is slightly increased. However, the increase or reduction of precipitable water vapor induced by dust, which accounts for less than 1% of the total amount of the precipitable water vapor in the atmosphere, is negligible.

The situation is different for the atmospheric ice water path. The atmospheric ice water path is lower than 1 g/m^2 over most of East Asia in the results of NO-DUST/CLOUD (Figure 7d), indicating that the production of ice crystals, or ice clouds, in the atmosphere is rare in the simulation without dust. By contrast, the atmospheric ice water path produced by DUST/CLOUD is substantially higher than that produced by NO-DUST/CLOUD over the entire simulation domain, with values higher than 20 g/m^2 over much of East Asia (Figure 7e). This corresponding to an increase of one order over vast areas, from dust source regions to the Northwest Pacific (Figure 7f), due to the dust particles serving as IN in the atmosphere. Dust nuclei in the atmosphere enable the super-cooled water droplets to freeze into ice crystals at a much higher temperature and lower relative humidity.

The spatial distribution for the mean atmospheric cloud water path over the entire simulation period from NO-DUST/CLOUD is shown in Figure 7g, in which the cloud water path is concentrated over South China and the West

338   Pacific, with values as high as 100 g/m^2. The spatial pattern of the atmospheric cloud water path from DUST/CLOUD

339   in Figure 7h is qualitatively similar to that from NO-DUST/CLOUD, but with much lower values. The comparison of

340   atmospheric cloud water paths between DUST/CLOUD and NO-DUST/CLOUD in Figure 7i shows that the

341   atmospheric cloud water path is reduced by more than 30 g/m^2 over south China, which accounts for one third of the

342   total atmospheric cloud water vapor over this region in the results of NO-DUST/CLOUD.

343   Figure 8 shows the spatial distributions for the mean simulated ice crystal number density and cloud droplet number

344   density produced by NO-DUST/CLOUD and DUST/CLOUD over East Asia during the entire simulation period, as

345   well as the difference between the results from the two simulations (DUST/CLOUD − NO-DUST/CLOUD). Similar

346   to the case in Figure 8, the simulated ice crystal number density increases substantially when the ice nucleation process

347   is enhanced by dust particles serving as IN. Compared with that produced by NO-DUST/CLOUD (Figure 8a), the ice

348   crystal number density produced by DUST/CLOUD (Figure 8b) is one order higher over the simulation domain as a

349   whole, and increased by as much as 6×10^8 /m^2 over north China and the south part of the ocean area. By contrast, the

350   simulated cloud droplet number density produced by DUST/CLOUD (Figure 8e) is much lower than that produced

351   by NO-DUST/CLOUD (Figure 8d). In DUST/CLOUD, the effects of dust reduce the cloud droplet number density

352   by around one third over this region compared with NO-DUST/CLOUD (Figure 8f).

353

354   **4.2.2 Vertical profile**

355   As the spatial distributions of the ice water path and cloud water path over East Asia are altered by the effects of dust,

356   the cloud ice mixing ratio and cloud water mixing ratio are also modified vertically. Figure 9 shows the vertical profiles

357   of the cloud ice and cloud water mixing ratios under the combined effects of dust. Note that the vertical profiles over

358   land, over the ocean, and over the entire simulation domain for East Asia are averaged across the whole simulation

359   period.

360   Due to the effects of dust, the cloud ice mixing ratio is increased at all altitudes from the near-surface layer to higher

361   than 15 km over the whole of East Asia, with two peaks located at 12 km and 6 km, as shown in Figure 9a. The smaller

362   peak at 6 km is due to the enhanced cloud ice mixing ratio over land. The cloud ice mixing ratio is uniformly increased

363   between 4 km and 13 km over land (Figure 9b), which results from the increase of IN served by the abundant dust

364   particles in the atmosphere. In contrast, the increase of the cloud ice mixing ratio over the ocean from 7 km to 15 km,

365   with a significant peak located at 12 km (Figure 9c). The enhancement of cloud ice mixing ratio over the ocean is

366 much greater than over land, likely due to more water vapor over the ocean. As noted above, the enhancement of the

367 cloud ice mixing ratio over the ocean also occurs at a higher altitude (7 km to 15 km) than that over land. A possible

368 cause of this difference is that only those particles fined enough to be lifted to high altitudes can be transported as far

369 as the open ocean of the West Pacific, whereas over land, more dust particles with larger sizes are suspended in lower

370 layers before settling down to the surface.

371 The vertical modification of the cloud water mixing ratio due to the effects of dust is fundamentally different from

372 that of cloud ice mixing ratio. Due to the effects of dust, the cloud water mixing ratio at low layers from the near-

373 surface to 3 km decreases over the whole of East Asia, with the average decrease peaking at around 1.5 km (Figure

374 9d). The overall decrease is dominated by the reduction in the cloud water mixing ratio over the ocean (Figure 9f).

375 The cloud water mixing ratio is also decreased over land at the same layers (Figure 9e), but by smaller magnitudes

376 compared with the decrease over the ocean. The vertical modification of the cloud water mixing ratio suggests that

377 the effects of dust is the significantly reduce low clouds over East Asia, especially over the ocean, where there is much

378 more abundant water vapor for cloud formation.

379 To summarize Section 4.2, the effects of dust result in a general increase of cloud ice and decrease of cloud water over

380 East Asia as a whole, whereby the increase in cloud ice is mainly concentrated at the mid- to upper troposphere, while

381 the decrease of cloud water mostly occurs in low clouds.

382 The increase in cloud formation at the mid- to upper troposphere is attributed to the indirect effect of dust. The

383 abundant IN in the atmosphere served by dust particles substantially increase the amount of ice crystals in mixed-

384 phase and ice clouds at these altitudes. In contrast, the decrease of low clouds is the result of two factors. One is the

385 warming within the atmosphere induced by the dust, leading to a much higher saturation pressure required for

386 atmospheric water vapor to form clouds, and a much faster evaporation rate of cloud droplets, which is due to the

387 cloud burning effect of dust. The other factor is that the super-cooled cloud droplets in the upper layers of the

388 troposphere freeze into ice crystals at a much higher temperature and lower relative humidity when dust particles serve

389 as IN in the atmosphere, leading to an increase of atmospheric ice water path. Given an approximately constant total

390 amount of water vapor in the atmosphere, the increased formation of ice crystals by the freezing of cloud droplets

391 results in a reduction in the amount of liquid cloud, and thus the atmospheric cloud water path, over East Asia as a

392 whole. The redistribution of atmospheric water vapor further strengthens the cloud radiative effect and modifies the

393 radiation budget over East Asia, as discussed in Section 4.1.2.

394

4.3 Vertical temperature profile

Due to the radiative forcing directly induced by dust discussed in Section 4.1.1, and the cloud radiative effect enhanced

by dust discussed in Section 4.1.2, the vertical temperature profile is modified. Figure 10 shows the modifications of

the vertical temperature profiles induced by the direct radiative effect of dust, the cloud radiative effect enhanced by

dust, and the full radiative effect of dust over the whole of East Asia, over land, and over the ocean during the

investigated period.

On average, the temperature over the simulation domain as a whole is slightly increased in the near-surface atmosphere,

decreased from 1 km to 3 km, increased significantly from 1 km up to 13 km, and then decreased above 13 km (Figure

10a). The contributions of the direct radiative effect of dust and dust-enhanced cloud radiative effect to the vertical

temperature modification are shown in Figure 10b and c. The direct radiative effect of dust (Figure 10b) results in a

decrease of temperature at the near-surface layer, and an increase above 1 km. In contrast, the pattern of the vertical

temperature modification caused by dust-enhanced cloud radiative effect (Figure 10c) is similar to that caused by the

full effect of dust, and is one order of magnitude larger magnitude than that caused by the direct radiative effect of

dust.

As the radiative forcing induced by dust over land differs from that over the ocean, the effects on the vertical

temperature profile requires further discussion. The decrease in temperature at the lower level of the troposphere

mainly occurs over land. The temperature over land decreases significantly below 2 km, then increases gradually from

2 km to 12 km, and decreases again over 12 km (Figure 10d). The decrease in temperature at the lower level is

composed of roughly equal contributions from the direct radiative effect and the dust-enhanced cloud radiative effect.

However, the increase in the temperature between 2 km and 12 km is mainly attributable to the dust-enhanced cloud

radiative effect (Figure 10f), the contribution of which is one order larger than that of the direct radiative effect of dust

(Figure 10e). The decrease in temperature at lower layers is mainly attributable to the negative SW radiative forcing

at the surface induced by dust, and the increase of temperature at the mid- to upper troposphere is due to the absorption

of LW radiation by dust-enhanced ice clouds.

The modification of the vertical temperature profile over the ocean is similar to that over East Asia as a whole,

especially at lower layers from the surface to 3 km, with an increase in temperature at the near-surface below 2 km,

and a decrease in temperature from 1 km to 3 km (Figure 10g). The direct radiative effect of dust results in a slight

422   decrease in temperature at the surface and at altitudes from 7 km to 9 km, but a slight increase from 1 km to 7 km and

423   above 10 km (Figure 10h). The dust-enhanced cloud radiative effect causes an overall increase in temperature from

424   the surface to 13 km, with a minor peak at an altitude of 1 km and a major peak at an altitude of 11 km (Figure 10i).

425   The modification of the vertical temperature profile over the ocean is mostly contributed by the dust-enhanced cloud

426   radiative effect over the ocean, with an almost identical pattern and magnitude to the temperature variation over East

427   Asia as a whole (Figure 10i).

428   The patterns of vertical temperature modification over land and ocean are due to different mechanisms. The vertical

429   temperature profile over land is chiefly modified by the direct radiative effect of dust at lower layers, and by the

430   enhanced cloud radiative effect due to the greater amount of ice clouds at the mid- to upper troposphere. With a heavier

431   dust burden over land, the SW radiation is blocked more effectively from reaching the land surface than the ocean

432   surface. Furthermore, the temperature at the near-surface layer over land responds to the SW radiation much faster

433   than that over the ocean, leading to a greater temperature decrease at lower levels over land. In the mid- to upper

434   troposphere, the greater amount of ice cloud leads to greater absorption of LW radiation emitted by the Earth, and the

435   enhanced freezing of cloud droplets into ice crystals promotes the release of latent heat, leading to a significant

436   increase of temperature in the surrounding atmosphere. The decrease in temperature below 2 km and the increase in

437   temperature above 2 km are likely to reduce atmospheric instability, which in turn will weakens the convective

438   motions over land.

439   The mechanism for the modification of the vertical temperature profile over the ocean is more complicated. As

440   discussed in Section 4.2, the effects of dust result in a substantial reduction of clouds, especially low clouds, and a

441   marked increase of ice clouds at the mid- to upper troposphere over the ocean. As ice clouds are much less efficient

442   in blocking solar radiation than low clouds, the reduction of low clouds leads to an increase of SW radiation over the

443   ocean, which heats up the ocean surface and near-surface layer of the atmosphere. Conversely, the reduction of low

444   clouds between 1 km and 3 km results in less LW radiation being absorbed by low clouds, and also less latent heat

445   being released by the condensation of water vapor into cloud droplets, both of which lead to a significant decrease of

446   temperature at layers between 1 km and 3 km. The increase in temperature above 3 km has the same cause as that over

447   land. The greater amount of ice clouds in the mid- to upper troposphere is able to absorb more of the LW radiation

448   emitted by the Earth, and the enhanced freezing of cloud droplets into ice crystals promotes the release of latent heat

449   into the surrounding atmosphere, leading to a significant increase in temperature in these layers. The cooling below 1

450 km and warming between 1 km and 3 km are likely to enhance atmospheric instability, causing stronger convective

451 motions over the ocean.

452

453 **4.4 Atmospheric stability**

454 As discussed above, the radiative forcing and the re-distribution of atmospheric water content induced by dust result

455 in a modification of the vertical temperature profile over East Asia. The corresponding shift of the thermal energy in

456 the atmosphere eventually lead to a modification of the atmospheric stability over this region.

457 The K-index (*KI*) is a metric widely used in meteorology to evaluate atmospheric stability, and is calculated with the

458 following equation (George, 2014):

459 $$KI = T_{850} - T_{500} + Td_{850} - (T_{700} - Td_{700}) \qquad (10)$$

460 where T_{850}, T_{700}, and T_{500} are the respective temperatures at 850 hPa, 700 hPa, and 500 hPa, and Td_{850} and Td_{700}

461 are the dew points at 850 hPa and 700 hPa. The calculation of *KI* considers the atmospheric stability as a function of

462 the vertical temperature lapse rate, the moisture content of the lower atmosphere, and the vertical extent of the moist

463 layer. The larger the value of *KI*, the more unstable the atmosphere. To evaluate the effect of dust on atmospheric

464 stability, *KI* was calculated from the simulation outputs.

465 Figure 11 shows the spatial distributions for the mean *KI* from NO-DUST/CLOUD over East Asia during the

466 simulation period, which represents the intrinsic average atmospheric stability free from the effects of dust, and Figure

467 12 shows the spatial distributions for the mean difference in *KI* between DUST/NO-CLOUD and NO-DUST/NO-

468 CLOUD (Figure 12a), between DUST/CLOUD and NO-DUST/CLOUD (Figure 12b), and between DUST/CLOUD

469 and NO-DUST/ CLOUD (Figure 12c). The differences represent the modification in *KI* induced by the direct radiative

470 effect of dust in Figure 12a, semi-direct and indirect effects, including cloud radiative effects and re-distribution of

471 atmospheric water content enhanced by dust, in Figure 12b, and the combined effects of the previous two in Figure

472 12c.

473 As shown in Figure 11, the mean *KI* over East Asia is lower in the north and increases gradually from north to south,

474 with the highest values located over the South China Sea and Southeast Asia, and the lowest values over the Central

475 to North Pacific.

476 Under the full effects of dust, the mean modification of *KI* over most land areas in East Asia is a significant decrease.

477 The largest decrease occurs over the dust source regions and central to East China (Figure 12c), and results from the

478   vertical modification over land. In contrast, *KI* significantly increases over most areas of the ocean and South China,

479   due to the different effects of dust on the vertical temperature over these areas, as discussed in Section 4.3. The

480   contributions of the direct radiative effect of dust and the indirect effects of dust on the modification of the mean *KI*

481   are shown in Figure 12a and b. The direct radiative effect of dust is to inhibit the atmospheric instability is inhibited

482   over most land areas, indicated by a significant decrease of the mean *KI*, as shown in Figure 12a. However, the overall

483   modification of mean *KI* is even greater over the ocean when the semi-direct and indirect effects of dust are taken into

484   account. Upon considering the semi-direct and indirect effects of dust, the modification of *KI* is much greater over

485   areas with more water vapor in the simulation domain, such as South China and most ocean areas, as shown in Figure

486   12b.

487   Overall, the atmosphere is significantly stabilized over the dust source regions and central to East China, but

488   significantly destabilized over South China and most ocean areas, due to the effects of dust. The dust-enhanced cloud

489   radiative forcing and the re-distribution of atmospheric water content due to dust contribute much more to the

490   modification of atmospheric stability than the direct radiative effect of dust does, especially over areas with abundant

491   water vapor.

492

493   **4.5 Precipitation**

494   The modification of atmospheric stability and re-distribution of atmospheric water content induced by dust eventually

495   alter the precipitation over East Asia. The spatial distributions for the mean precipitation rate, including total

496   precipitation, convective precipitation, and non-convective precipitation from NO-DUST/CLOUD and

497   DUST/CLOUD, as well as the difference between the two simulations, are shown in Figure 13. Note that the

498   precipitation rate shown in Figure 14 is the mean daily precipitation rate averaged over the simulation period.

499   The spatial pattern of the mean total precipitation rate from NO-DUST/CLOUD shown in Figure 13a is generally

500   similar to that from DUST/CLOUD shown in Figure 13b. However, as discussed in Section 3.2.2, the simulated

501   precipitation center produced in NO-DUST/NO-CLOUD spans an area from Hunan to Jiangxi (Figure 13a), to the

502   north of the observed precipitation, and the simulated precipitation rate over South China is significantly lower than

503   the observational values. By contrast, in DUST/CLOUD (Figure 13b), the precipitation band from Hunan to Jiangxi

504   is markedly inhibited, while the precipitation rate over South China is enhanced, which is clearly more consistent with

505   the observations. As shown in Figure 13c, the total precipitation is reduced by as much as 1 mm/day or more over

506   most land areas, but increased by up to 1 mm/day over South China, due to the effects of dust. The modifications in

507   precipitation account for over 20% of the total simulated precipitation rate over both land and the ocean.

508   The simulated convective precipitation mostly occurs over the southern part of the simulation domain, with

509   precipitation centers located over central to East China, South China, the South China Sea, and Southeast Asia (Figure

510   13d and e). The total precipitation over these areas is chiefly affected by the modification of convective precipitation.

511   Due to the effects of dust, convective precipitation is significantly reduced at the precipitation center from central to

512   East China, but substantially enhanced over South China and the ocean (Figure 13f). The inhibition of convective

513   precipitation over Central to East China has two reasons. One is the general enhancement of atmospheric stability,

514   which reduces the convective motion over this region. The other is the decrease in low clouds over South China and

515   the ocean, which reduces the availability of cloud droplets that can grow into rain droplets under the same

516   meteorological conditions. The greater convective precipitation over South China is due to the greater atmospheric

517   instability, which promotes convective motions.

518   The simulated non-convective precipitation is produced by the microphysics scheme. The Non-convective

519   precipitation mainly occurs at the western rim of the Taklimakan Desert, northeast China, Japan, and the areas between

520   27°N and 36°N over East Asia during the simulation period. The non-convective precipitation rate produced in

521   DUST/CLOUD (Figure 13h) is markedly lower than that produced in NO-DUST/CLOUD (Figure 13g) at the northern

522   precipitation centers. Figure 13i shows that the non-convective precipitation rate is reduced by more than 30% at the

523   western of the Taklimakan Desert and in the rain band from East China to Japan. More super-cooled water droplets

524   can freeze into ice crystals in the upper troposphere due to the abundant IN served by dust particles, leading to much

525   lower atmospheric cloud water content and cloud droplet number concentration directly above the non-convective

526   precipitation center. Furthermore, the warming within the atmosphere, which is caused by radiative forcing and latent

527   heat released by the freezing of super-cooled water droplets, results in a higher saturation pressure for water vapor

528   and faster evaporation rate for cloud droplets. This, in turn, suppresses the growth of cloud droplets into rain droplets,

529   leading to an inhibition of non-convective precipitation. Conversely, the increase in cloud ice in some cases leads to

530   more precipitation. The ice crystals in mixed-phase clouds can grow large enough to induce precipitation given

531   sufficient water vapor in the atmosphere. An example is the enhancement of non-convective precipitation over the

532   East China Sea.

533

5 Conclusions

By applying the updated WRF-Chem, which is capable of evaluating indirect effect of dust along with the direct and semi-direct effect in dust simulations, the full effects of dust, including direct radiative, cloud radiative, and indirect microphysical effects, on the meteorological field over East Asia during March and April 2012 were quantified and discussed.

For the radiative forcing induced by dust, the direct radiative effect of dust combined with the dust-enhanced cloud radiative effect causes a net loss of radiation at the Earth's surface, but a net gain of radiation within the atmosphere, leading to cooling at the surface and lower troposphere, and warming in the mid- to upper troposphere. The radiative forcing caused by the dust-enhanced cloud radiative effect is much greater than that caused by the direct radiative effect of dust, especially for LW radiative forcing, which is highly affected by cloud cover. The LW radiative forcing caused by the dust-enhanced cloud radiative effect is one order stronger than that cased by the direct radiative effect of dust at the top of the atmosphere and within the atmosphere. The spatial distribution of radiative forcing further implies a shift of the spatial distribution of cloud cover, such that the cloud cover is likely increased over land, but reduced over the ocean, due to the presence of dust, indicating a re-distribution of atmospheric water vapor over East Asia.

The atmospheric ice water path and ice crystal number density are significantly increased over East Asia, when abundant dust particles are available to serve as IN. By contrast, the atmospheric cloud water path and cloud droplet number density are substantially reduced. Vertically, the effects of dust result in a general increase of cloud ice and decrease of cloud water over East Asia as a whole, whereby the increase of cloud ice is mainly concentrated at the mid- to upper troposphere, while the decrease in cloud water mostly occurs in low clouds. The increase in clouds at the mid- to upper troposphere is due to the indirect effect of dust by serving as IN. The reduction in low clouds is attributed to two factors. One is the semi-direct effect of dust. Dust particles within clouds absorb radiation and warm up the surrounding environment, leading to a much greater saturation pressure required for atmospheric water vapor to form clouds, and a much faster evaporation rate of cloud droplets. The other factor is that the ice nucleation process enhanced by dust facilitates the freezing of atmospheric super-cooled water droplets into ice crystals.

The radiative forcing and re-distribution of atmospheric water vapor induced by dust lead to a modification of the vertical temperature profile. Consequently, the atmosphere is stabilized over most land areas, but destabilized over most of the ocean in East Asia. The cloud radiative forcing enhanced by dust and the re-distribution of atmospheric

562 water content due to dust contribute much more to the modification of atmospheric stability than the direct radiative

563 effect of dust does.

564 Convective precipitation is inhibited over most land areas in East Asia, because of the enhanced atmospheric stability,

565 and the reduction in cloud droplets capable of growing into rain droplets under atmospheric conditions. Conversely,

566 convective precipitation is enhanced over South China and the ocean due to the greater atmospheric instability over

567 these areas. The presence of much fewer cloud droplets in the atmosphere, combined with the atmospheric warming

568 caused by radiative forcing and the release of latent heat by the freezing of super-cooled water droplets, results in a

569 higher saturation pressure for water vapor and faster evaporation rate for cloud droplets, which in turn inhibit non-

570 convective precipitation. The decrease in convective and non-convective precipitation results in a reduction of total

571 precipitation over East Asia. Nevertheless, the increase of cloud ice also leads to more precipitation in some cases.

572 The ice crystals in mixed-phase clouds can grow large enough to induce a precipitation given sufficient atmospheric

573 water vapor.

574

575 **Acknowledgement.** We would like to acknowledge the principle investigators and their staff from Data Assimilation

576 and Modeling Center for Tibetan Multi-spheres, Institute of Tibetan Plateau Research, Chinese Academy of Sciences,

577 for provision of the China Meteorological Forcing Dataset used in this study for model validation. The dataset can be

578 found online at http://westdc.westgis.ac.cn/data/7a35329c-c53f-4267-aa07-e0037d913a21. Lin Su would like to thank

579 Dr. Georg Grell, Dr. Stuart McKeen, and Dr. Ravan Ahmandov from the Earth System Research Laboratory, U.S.

580 National Oceanic and Atmospheric Administration for insightful discussions. All data used in this paper are properly

581 cited and referred to in the reference list. All data shown in the results are available upon request. This work was

582 supported by NSFC/RGC Grant N_HKUST631/05, NSFC-FD Grant U1033001, and the RGC Grant 16303416.

583

References

Atkinson, J. D., Murray, B. J., Woodhouse, M. T., Whale, T. F., Baustian, K. J., Carslaw, K. S., Dobbie, S., O'sullivan, D., and Malkin, T. L.: The importance of feldspar for ice nucleation by mineral dust inmixed-phase clouds, Nature, 498, 355, 2013.

Bi, J., Huang, J., Fu, Q., Ge, J., Shi, J., Zhou, T., and Zhang, W.: Field measurement of clear-sky solar irradiance in Badain Jaran Desert of Northwestern China, Journal of Quantitative Spectroscopy and Radiative Transfer, 122, 194-207, 2013.

Broadley, S., Murray, B., Herbert, R., Atkinson, J., Dobbie, S., Malkin, T., Condliffe, E., and Neve, L.: Immersion mode heterogeneous ice nucleation by an illite rich powder representative of atmospheric mineral dust, Atmospheric Chemistry and Physics, 12, 287-307, 2012.

Chen, Y., Yang, K., He, J., Qin, J., Shi, J., Du, J., and He, Q.: Improving land surface temperature modeling for dry land of China, Journal of Geophysical Research: Atmospheres, 116, 2011.

Connolly, P., Möhler, O., Field, P., Saathoff, H., Burgess, R., Choularton, T., and Gallagher, M.: Studies of heterogeneous freezing by three different desert dust samples, Atmospheric Chemistry and Physics, 9, 2805-2824, 2009.

DeMott, P. J., Sassen, K., Poellot, M. R., Baumgardner, D., Rogers, D. C., Brooks, S. D., Prenni, A. J., and Kreidenweis, S. M.: African dust aerosols as atmospheric ice nuclei, Geophysical Research Letters, 30, 2003.

DeMott, P. J., Prenni, A. J., McMeeking, G. R., Sullivan, R. C., Petters, M. D., Tobo, Y., Niemand, M., Möhler, O., Snider, J. R., and Wang, Z.: Integrating laboratory and field data to quantify the immersion freezing ice nucleation activity of mineral dust particles, Atmospheric Chemistry and Physics, 15, 393-409, 2015.

Ge, J., Su, J., Ackerman, T., Fu, Q., Huang, J., and Shi, J.: Dust aerosol optical properties retrieval and radiative forcing over northwestern China during the 2008 China-US joint field experiment, Journal of Geophysical Research: Atmospheres, 115, 2010.

George, J. J.: Weather forecasting for aeronautics, Academic press, 2014.

Ginoux, P., Chin, M., Tegen, I., Prospero, J. M., Holben, B., Dubovik, O., and Lin, S. J.: Sources and distributions of dust aerosols simulated with the GOCART model, Journal of Geophysical Research: Atmospheres, 106, 20255-20273, 2001.

Ginoux, P., Prospero, J. M., Torres, O., and Chin, M.: Long-term simulation of global dust distribution with the

612 GOCART model: correlation with North Atlantic Oscillation, Environmental Modelling & Software, 19, 113-128,

613 2004.

614 Grell, Ahmadov, R., Peckham, S., Wong, K., Zhang, L., McKeen, S. A., Easter, R., Fast, J. D., Gustafson, W., Ma, P.

615 L., Singh, B., Hodzic, A., Batrth, M., Pfster, G., Wolters, S., Bella, M., Freitas, S. R., Tuccella, P., Zhang, Y., Wang,

616 K., and Klose, M.: WRF-Chem V3. 8: A summary of status and updates, EGU General Assembly Conference Abstracts,

617 2016.

618 Grell, G. A., and Freitas, S. R.: A scale and aerosol aware stochastic convective parameterization for weather and air

619 quality modeling, Atmos. Chem. Phys, 14, 5233-5250, 2014.

620 Hansen, J., Sato, M., and Ruedy, R.: Radiative forcing and climate response, Journal of Geophysical Research:

621 Atmospheres, 102, 6831-6864, 1997.

622 Hartmann, D., Tank, A., and Rusticucci, M.: IPCC fifth assessment report, climate change 2013: The physical science

623 basis, IPCC AR5, 31-39, 2013.

624 Hoose, C., Lohmann, U., Erdin, R., and Tegen, I.: The global influence of dust mineralogical composition on

625 heterogeneous ice nucleation in mixed-phase clouds, Environmental Research Letters, 3, 025003, 2008.

626 Huang, J., Fu, Q., Su, J., Tang, Q., Minnis, P., Hu, Y., Yi, Y., and Zhao, Q.: Taklimakan dust aerosol radiative heating

627 derived from CALIPSO observations using the Fu-Liou radiation model with CERES constraints, Atmospheric

628 Chemistry and Physics, 9, 4011-4021, 2009.

629 Huang, J.: Emission, transport, and radiative effects of mineral dust from the Taklimakan and Gobi deserts: comparison

630 of measurements and model results, Atmos. Chem. Phys, 1680, 7324, 2017.

631 Iacono, M. J., Delamere, J. S., Mlawer, E. J., Shephard, M. W., Clough, S. A., and Collins, W. D.: Radiative forcing

632 by long-lived greenhouse gases: Calculations with the AER radiative transfer models, Journal of Geophysical

633 Research: Atmospheres, 113, 2008.

634 Janjić, Z. I.: The step-mountain eta coordinate model: Further developments of the convection, viscous sublayer, and

635 turbulence closure schemes, Monthly Weather Review, 122, 927-945, 1994.

636 Janjić, Z. I.: Nonsingular implementation of the Mellor–Yamada level 2.5 scheme in the NCEP Meso model, NCEP

637 office note, 437, 61, 2002.

638 Karydis, V., Kumar, P., Barahona, D., Sokolik, I., and Nenes, A.: On the effect of dust particles on global cloud

639 condensation nuclei and cloud droplet number, Journal of Geophysical Research: Atmospheres, 116, 2011.

640 Koehler, K., Kreidenweis, S., DeMott, P., Petters, M., Prenni, A., and Möhler, O.: Laboratory investigations of the

641 impact of mineral dust aerosol on cold cloud formation, Atmospheric Chemistry and Physics, 10, 11955-11968, 2010.

642 Koop, T., Luo, B., Tsias, A., and Peter, T.: Water activity as the determinant for homogeneous ice nucleation in aqueous

643 solutions, Nature, 406, 611-614, 2000.

644 Lacis, A.: Climate forcing, climate sensitivity, and climate response: A radiative modeling perspective on atmospheric

645 aerosols, Aerosol forcing of climate, 11-42, 1995.

646 Liu, Huang, J., Shi, G., Takamura, T., Khatri, P., Bi, J., Shi, J., Wang, T., Wang, X., and Zhang, B.: Aerosol optical

647 properties and radiative effect determined from sky-radiometer over Loess Plateau of Northwest China, Atmospheric

648 Chemistry and Physics, 11, 11455-11463, 2011a.

649 Liu, Zheng, Y., Li, Z., Flynn, C., Welton, E. J., and Cribb, M.: Transport, vertical structure and radiative properties of

650 dust events in southeast China determined from ground and space sensors, Atmospheric environment, 45, 6469-6480,

651 2011b.

652 Lohmann, U., and Feichter, J.: Global indirect aerosol effects: a review, Atmospheric Chemistry and Physics, 5, 715-

653 737, 2005.

654 Lohmann, U., and Diehl, K.: Sensitivity studies of the importance of dust ice nuclei for the indirect aerosol effect on

655 stratiform mixed-phase clouds, Journal of the Atmospheric Sciences, 63, 968-982, 2006.

656 Mallet, M., Tulet, P., Serça, D., Solmon, F., Dubovik, O., Pelon, J., Pont, V., and Thouron, O.: Impact of dust aerosols

657 on the radiative budget, surface heat fluxes, heating rate profiles and convective activity over West Africa during

658 March 2006, Atmospheric Chemistry and Physics, 9, 7143-7160, 2009.

659 Mlawer, E. J., Taubman, S. J., Brown, P. D., Iacono, M. J., and Clough, S. A.: Radiative transfer for inhomogeneous

660 atmospheres: RRTM, a validated correlated-k model for the longwave, Journal of Geophysical Research: Atmospheres,

661 102, 16663-16682, 1997.

662 Nabat, P., Somot, S., Mallet, M., Michou, M., Sevault, F., Driouech, F., Meloni, D., Di Sarra, A., Di Biagio, C., and

663 Formenti, P.: Dust aerosol radiative effects during summer 2012 simulated with a coupled regional aerosol–

664 atmosphere–ocean model over the Mediterranean, Atmospheric Chemistry and Physics, 15, 3303-3326, 2015a.

665 Nabat, P., Somot, S., Mallet, M., Sevault, F., Chiacchio, M., and Wild, M.: Direct and semi-direct aerosol radiative

666 effect on the Mediterranean climate variability using a coupled regional climate system model, Climate dynamics, 44,

667 1127-1155, 2015b.

668 Palacios, L., Baró, R., and Jiménez-Guerrero, P.: An on-line modelling study of the direct effect of atmospheric

669 aerosols over Europe, Física de la Tierra, 27, 155, 2015.

670 Perlwitz, J., and Miller, R. L.: Cloud cover increase with increasing aerosol absorptivity: A counterexample to the

671 conventional semidirect aerosol effect, Journal of Geophysical Research: Atmospheres, 115, 2010.

672 Phillips, V. T., DeMott, P. J., and Andronache, C.: An empirical parameterization of heterogeneous ice nucleation for

673 multiple chemical species of aerosol, Journal of the atmospheric sciences, 65, 2757-2783, 2008.

674 Pinker, R., and Laszlo, I.: Modeling surface solar irradiance for satellite applications on a global scale, Journal of

675 Applied Meteorology, 31, 194-211, 1992.

676 Rodell, M., Houser, P., Jambor, U., Gottschalck, J., Mitchell, K., Meng, C., Arsenault, K., Cosgrove, B., Radakovich,

677 J., and Bosilovich, M.: The global land data assimilation system, Bulletin of the American Meteorological Society, 85,

678 381-394, 2004.

679 Sassen, K.: Indirect climate forcing over the western US from Asian dust storms, Geophysical Research Letters, 29,

680 2002.

681 Sassen, K., DeMott, P. J., Prospero, J. M., and Poellot, M. R.: Saharan dust storms and indirect aerosol effects on

682 clouds: CRYSTAL-FACE results, Geophysical Research Letters, 30, 2003.

683 Satheesh, S., Deepshikha, S., and Srinivasan, J.: Impact of dust aerosols on Earth–atmosphere clear-sky albedo and

684 its short wave radiative forcing over African and Arabian regions, International Journal of Remote Sensing, 27, 1691-

685 1706, 2006.

686 Seigel, R., Van Den Heever, S., and Saleeby, S.: Mineral dust indirect effects and cloud radiative feedbacks of a

687 simulated idealized nocturnal squall line, Atmospheric Chemistry and Physics, 13, 4467-4485, 2013.

688 Seinfeld, J. H., Carmichael, G. R., Arimoto, R., Conant, W. C., Brechtel, F. J., Bates, T. S., Cahill, T. A., Clarke, A. D.,

689 Doherty, S. J., and Flatau, P. J.: ACE-ASIA: Regional climatic and atmospheric chemical effects of Asian dust and

690 pollution, Bulletin of the American Meteorological Society, 85, 367-380, 2004.

691 Shao: Simplification of a dust emission scheme and comparison with data, Journal of Geophysical Research:

692 Atmospheres, 109, 2004.

693 Shao, Ishizuka, M., Mikami, M., and Leys, J.: Parameterization of size-resolved dust emission and validation with

694 measurements, Journal of Geophysical Research: Atmospheres, 116, 2011.

695 Sheffield, J., Goteti, G., and Wood, E. F.: Development of a 50-year high-resolution global dataset of meteorological

696 forcings for land surface modeling, Journal of Climate, 19, 3088-3111, 2006.

697 Solomon, S.: Climate change 2007-the physical science basis: Working group I contribution to the fourth assessment

698 report of the IPCC, Cambridge University Press, 2007.

699 Su, L., and Fung, J. C.: Sensitivities of WRF-Chem to dust emission schemes and land surface properties in simulating

700 dust cycles during springtime over East Asia, Journal of Geophysical Research: Atmospheres, 120, 2015.

701 Targino, A. C., Krejci, R., Noone, K. J., and Glantz, P.: Single particle analysis of ice crystal residuals observed in

702 orographic wave clouds over Scandinavia during INTACC experiment, Atmospheric Chemistry and Physics, 6, 1977-

703 1990, 2006.

704 Teller, A., and Levin, Z.: The effects of aerosols on precipitation and dimensions of subtropical clouds: a sensitivity

705 study using a numerical cloud model, Atmospheric Chemistry and Physics, 6, 67-80, 2006.

706 Tesfaye, M., Tsidu, G. M., Botai, J., and Sivakumar, V.: Mineral dust aerosol distributions, its direct and semi-direct

707 effects over South Africa based on regional climate model simulation, Journal of Arid Environments, 114, 22-40, 2015.

708 Thompson, G., and Eidhammer, T.: A study of aerosol impacts on clouds and precipitation development in a large

709 winter cyclone, Journal of the Atmospheric Sciences, 71, 3636-3658, 2014.

710 Wesely, M.: Parameterization of surface resistances to gaseous dry deposition in regional-scale numerical models,

711 Atmospheric Environment (1967), 23, 1293-1304, 1989.

712 Yang, K., He, J., Tang, W., Qin, J., and Cheng, C. C.: On downward shortwave and longwave radiations over high

713 altitude regions: Observation and modeling in the Tibetan Plateau, Agricultural and Forest Meteorology, 150, 38-46,

714 2010.

715 Zhang, C., Wang, M., Morrison, H., Somerville, R. C., Zhang, K., Liu, X., and Li, J. L. F.: Investigating ice nucleation

716 in cirrus clouds with an aerosol-enabled Multiscale Modeling Framework, Journal of Advances in Modeling Earth

717 Systems, 6, 998-1015, 2014.

718

719

748   simulation domain (a-c), over land (d-f), and over ocean (g-i).

749   Figure 11: Spatial distributions of the monthly average K-index from NO-DUST/CLOUD.

750   Figure 12: Spatial distributions of the modification of K-index induced by the direct radiative effect of dust (a), the

751   semi-direct and indirect effects of dust (b), and the full effects of dust (c).

752   Figure 13: Spatial distributions of the average simulated total precipitation rate (a-c), convective precipitation rate (d-

753   f), and non-convective precipitation rate (g-i) from NO-DUST/CLOUD (left panel), DUST/CLOUD (middle panel),

754   and the difference between DUST/CLOUD and NO-DUST/CLOUD (right panel).

755

756   **Table 1:** Model configurations for the numerical simulations.

Scheme \ Experiment	NO-DUST/NO-CLOUD	NO-DUST/CLOUD	DUST/NO-CLOUD	DUST/CLOUD
Dust emission scheme	----	----	Shao	Shao
Dry deposition	----	----	Gravitational settling/surface deposition	Gravitational settling/surface deposition
Wet deposition	----	----	In-cloud and below-cloud	In-cloud and below-cloud
Aerosol optical scheme	----	----	Maxwell-Garnett	Maxwell-Garnett
Aerosol radiative feedback	off	off	on	on
Cloud radiative feedback	off	on	off	on

757

Table 2: WRF-Chem-simulated SW, LW, and net radiative forcing (W/m^2) induced by dust over East Asia at TOA, BOT, and ATM.

	Clear-sky			All-sky		
	SW	LW	Net	SW	LW	Net
TOA (+down)	-1.22	0.02	-1.20	-7.81	9.52	1.70
ATM (+warm)	1.23	-1.07	0.15	0.06	9.26	9.33
BOT (+down)	-2.44	1.09	-1.36	-7.87	0.25	-7.62

SW: short-wave radiative forcing; LW: long-wave radiative forcing; Net: net radiative forcing.
TOA: radiative forcing at the top of the atmosphere; ATM: radiative effect within the atmosphere; BOT: radiative effect at the bottom of the atmosphere.
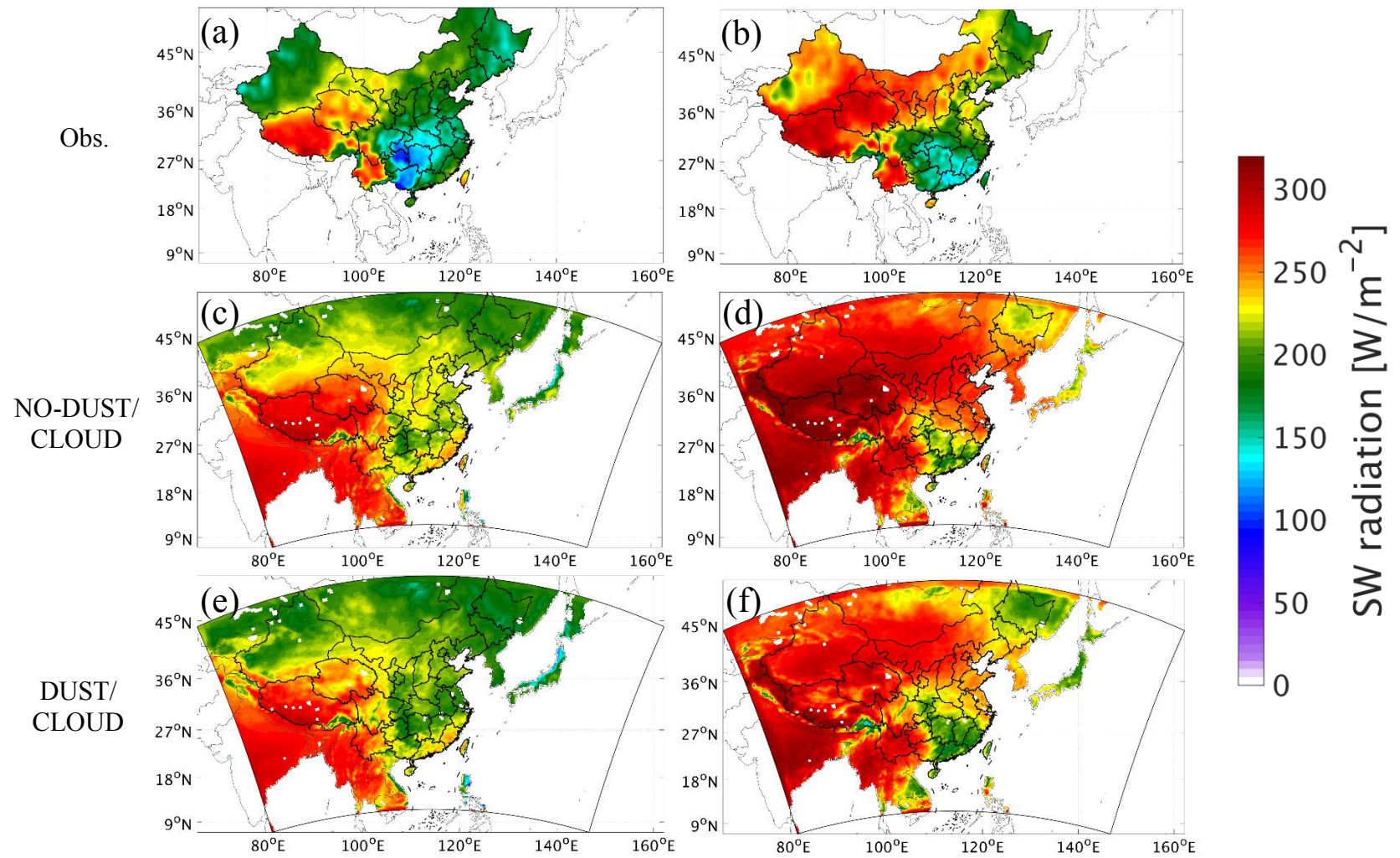
Figure 1: Spatial distributions of the average downward SW radiation at surface from observations (a, b), from NO-DUST/CLOUD (c, d), and from DUST-CLOUD (e, f) during March (left panel) and April (right panel) 2012.
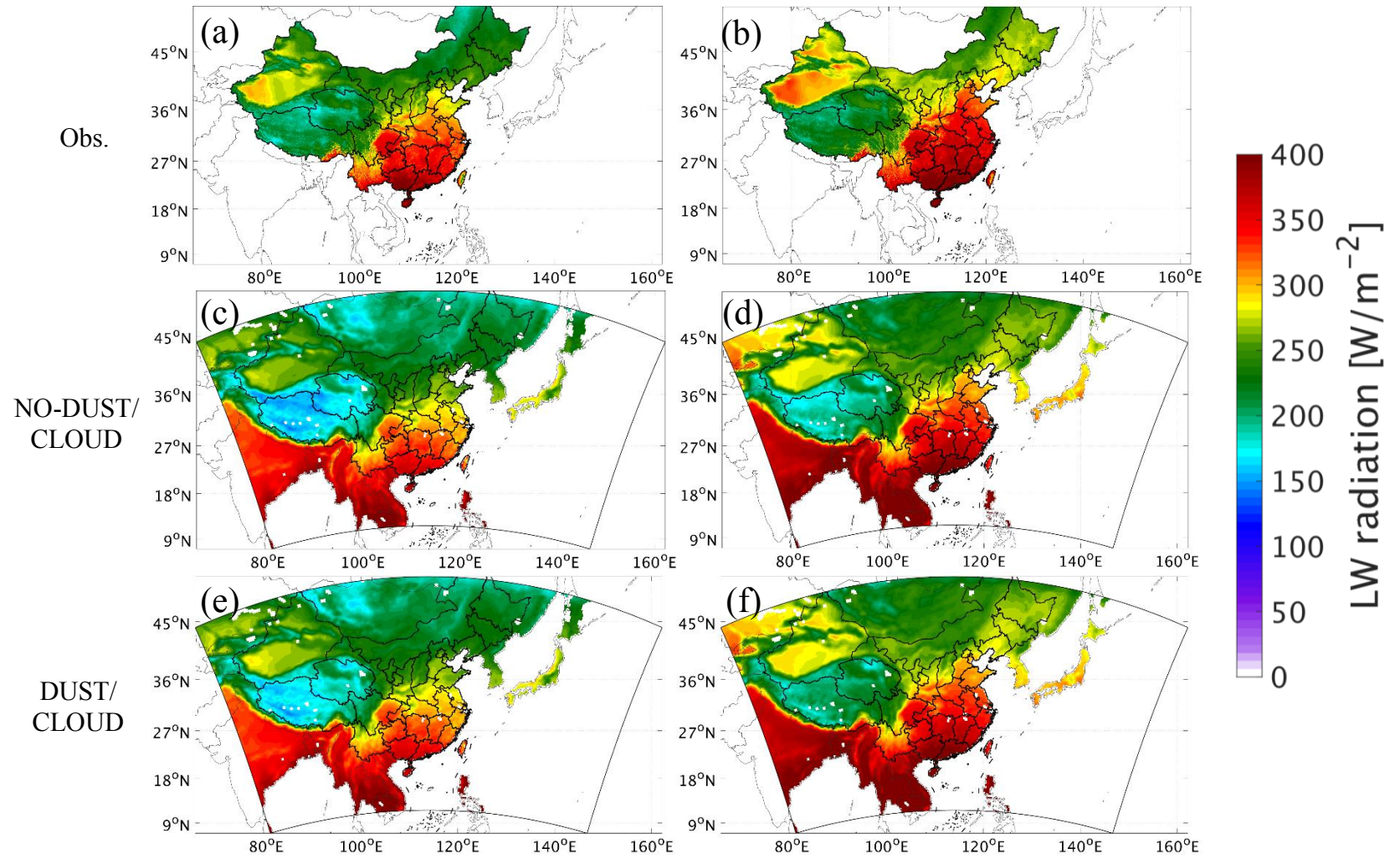
Figure 2: Spatial distributions of the average downward LW radiation at surface from observations (a, b), from NO-DUST/CLOUD (c, d), and from DUST-CLOUD (e, f) during March (left panel) and April (right panel) 2012.
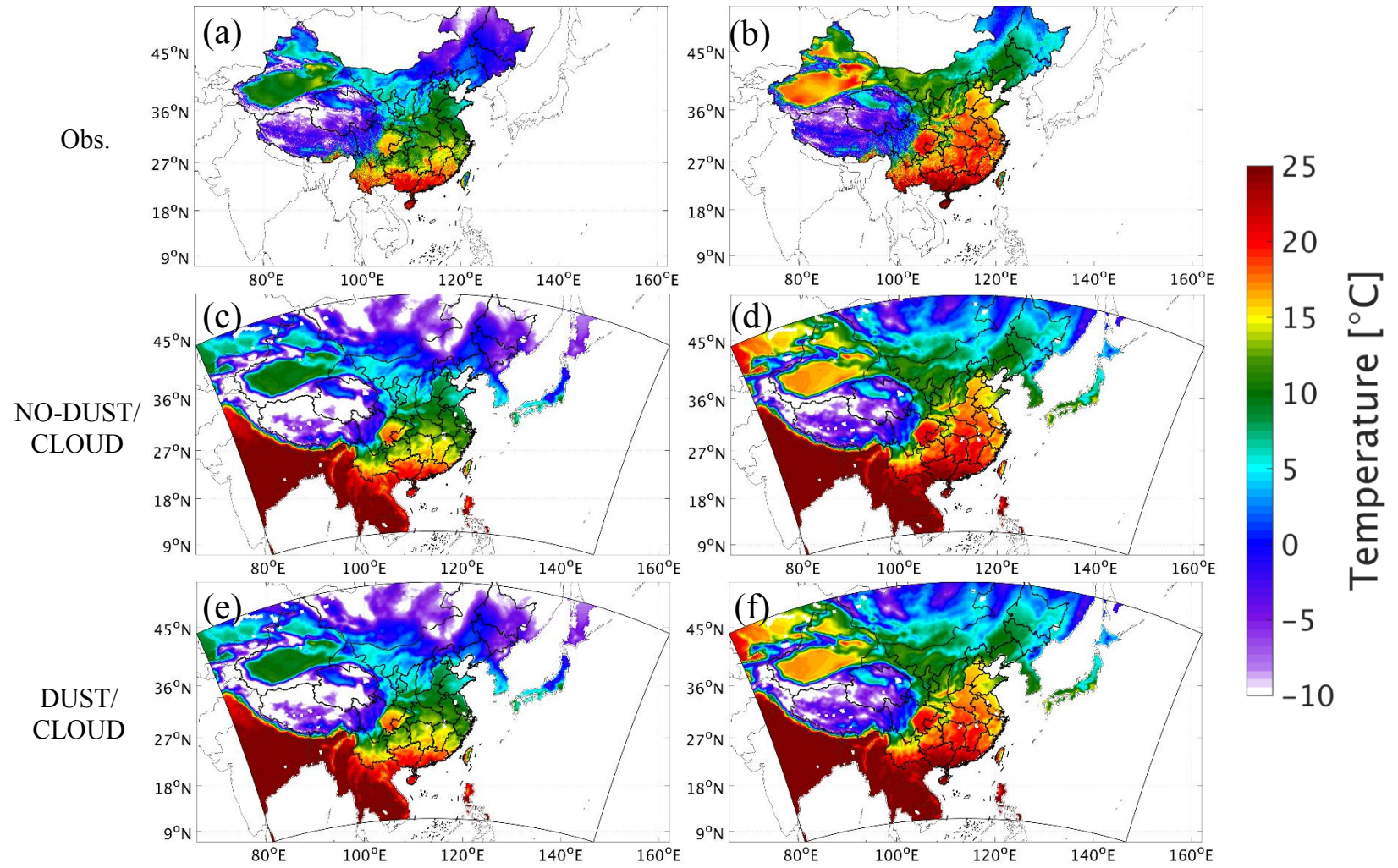
Figure 3: Spatial distributions of the average near-surface temperature from observations (a, b), from NO-DUST/CLOUD (c, d), and from DUST-CLOUD (e, f) during March (left panel) and April (right panel) 2012.
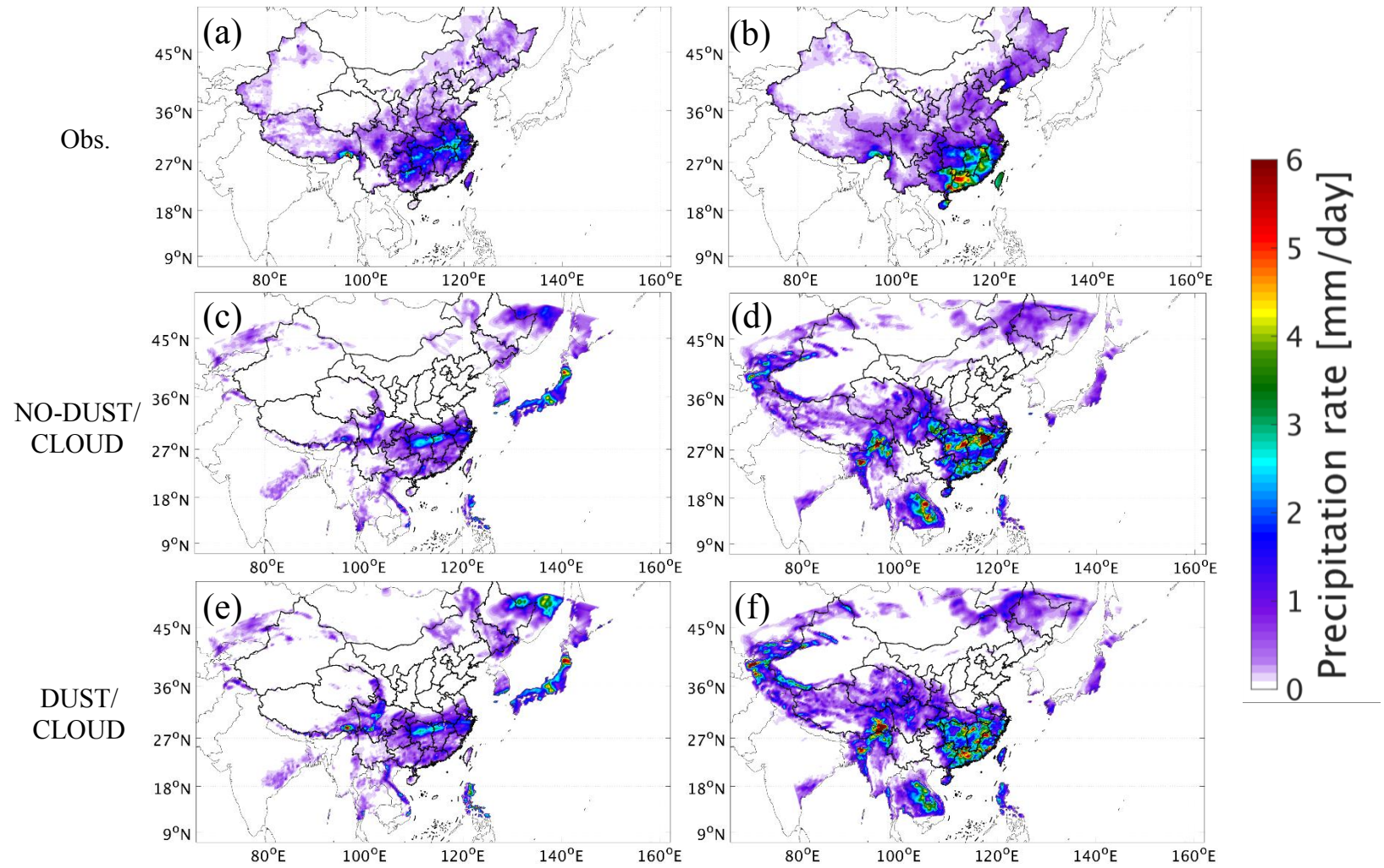
Figure 4: Spatial distributions of the average precipitation rate from observations (a, b), from NO-DUST/CLOUD (c, d), and from DUST/CLOUD (e, f) during March (left panel) and April (right panel) 2012.
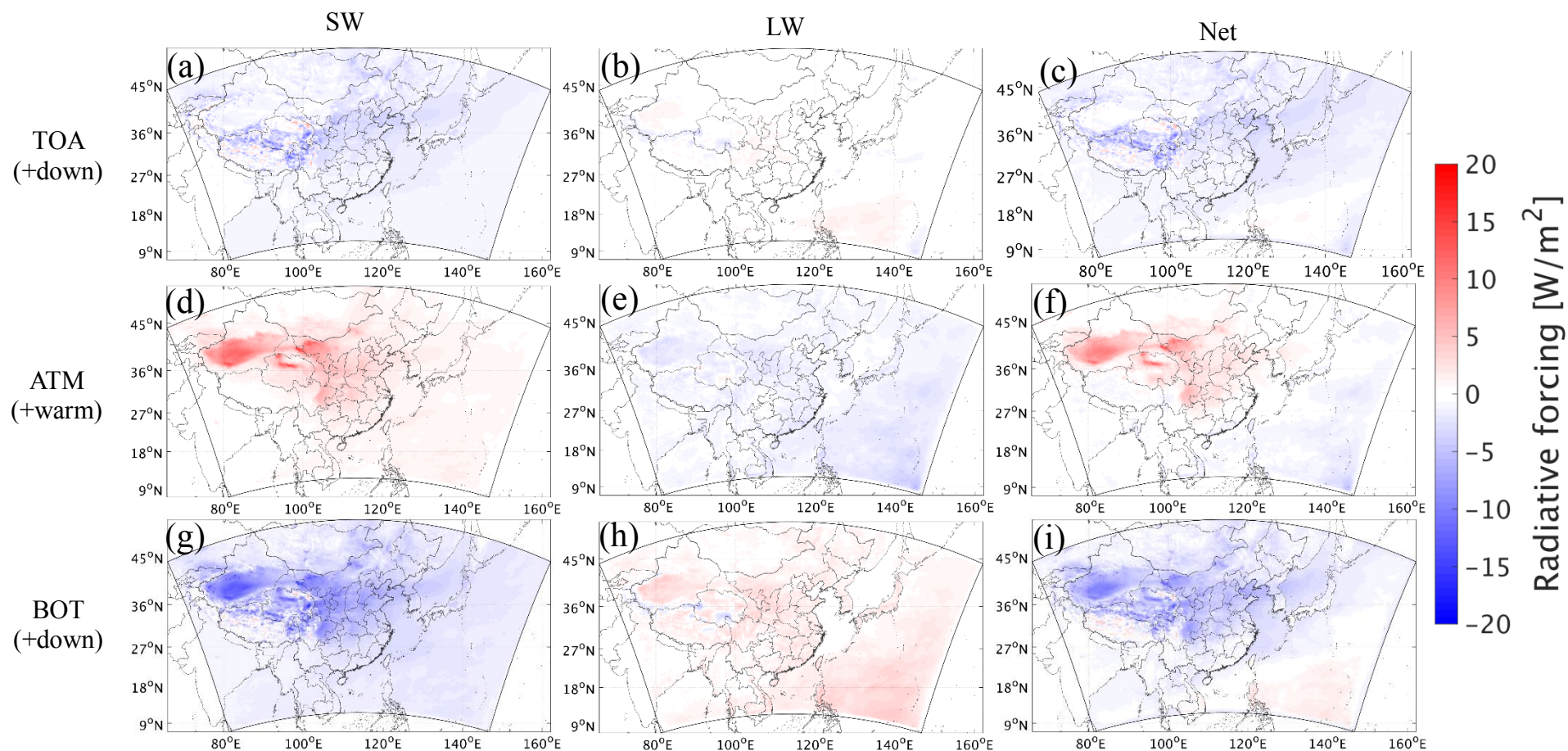
Figure 5: Spatial distributions of the clear-sky SW (left panel), LW (middle panel), and net (right panel) radiative forcing at the top of the atmosphere (TOA, a-c), within the atmosphere (ATM, d-f), and at the bottom of the atmosphere (BOT, g-i).
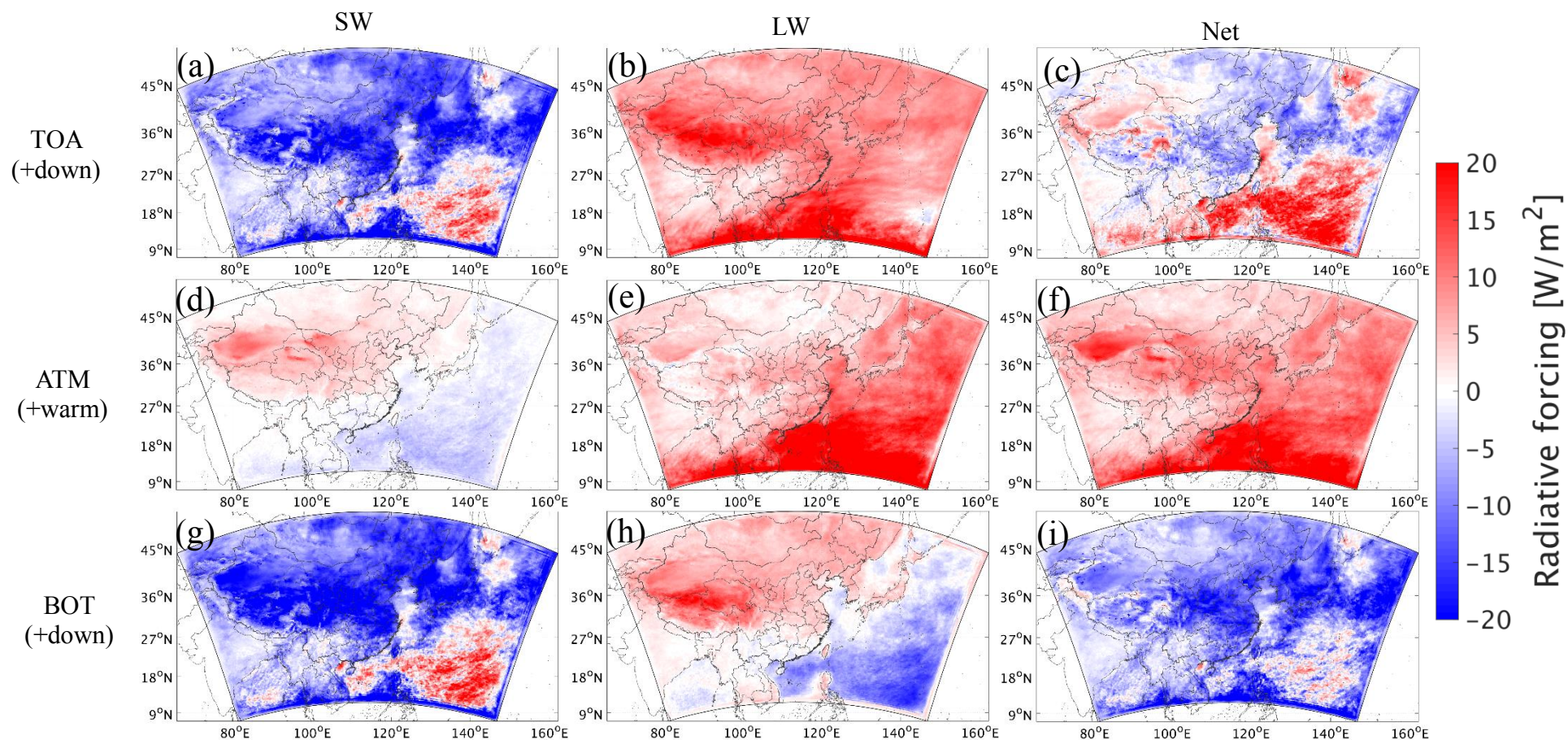
Figure 6: Spatial distributions of the all-sky SW (left panel), LW (middle panel), and net (right panel) radiative forcing at the top of the atmosphere (TOA, a-c), within the atmosphere (ATM, d-f), and at the bottom of the atmosphere (BOT, g-i).
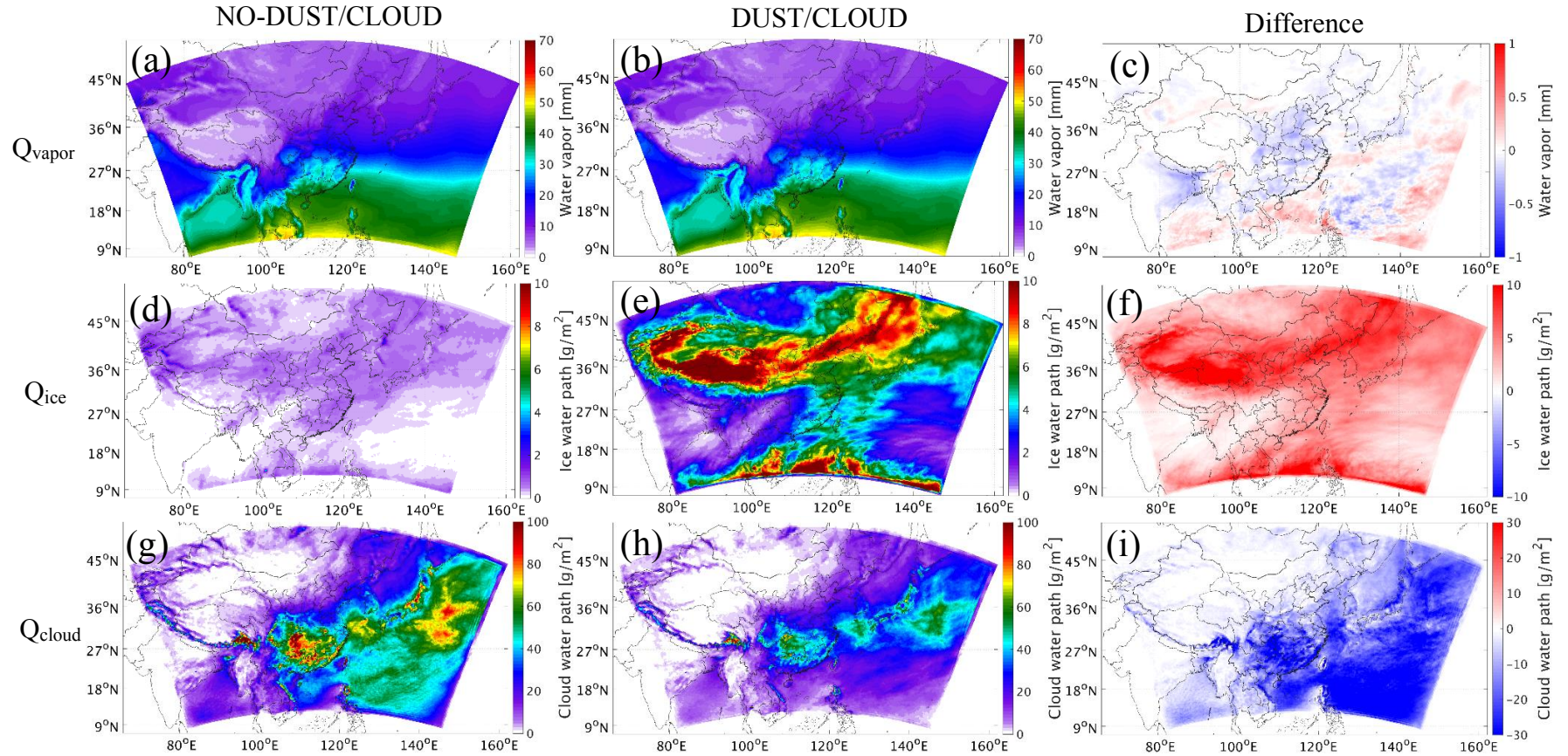
Figure 7: Spatial distributions of the average simulated precipitable water vapor (a-c), ice water path (d-f), and cloud water path (g-i) from NO-DUST/CLOUD (left panel), DUST/CLOUD (middle panel), and difference between DUST/CLOUD and NO-DUST/CLOUD (right panel).
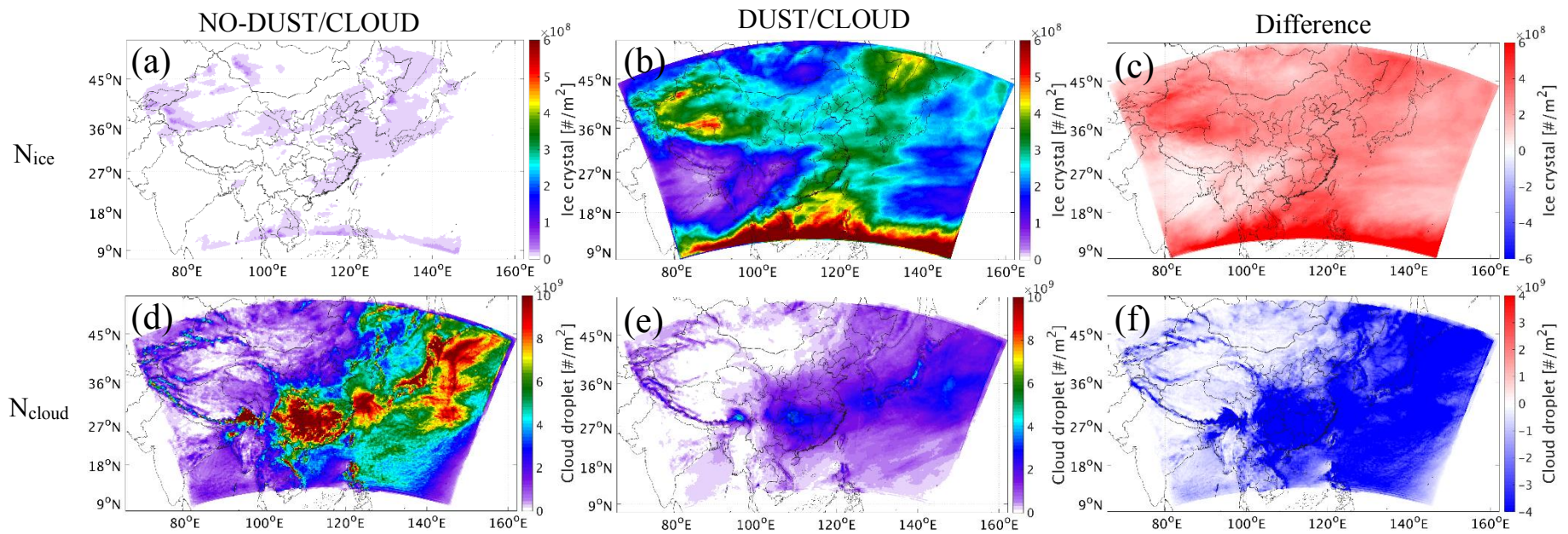
Figure 8: Spatial distributions of the average simulated ice crystal number density (a-c) and cloud droplet number density (d-f) from NO-DUST/CLOUD (left panel), DUST/CLOUD (middle panel), and difference between DUST/CLOUD and NO-DUST/NO-CLOUD (right panel).
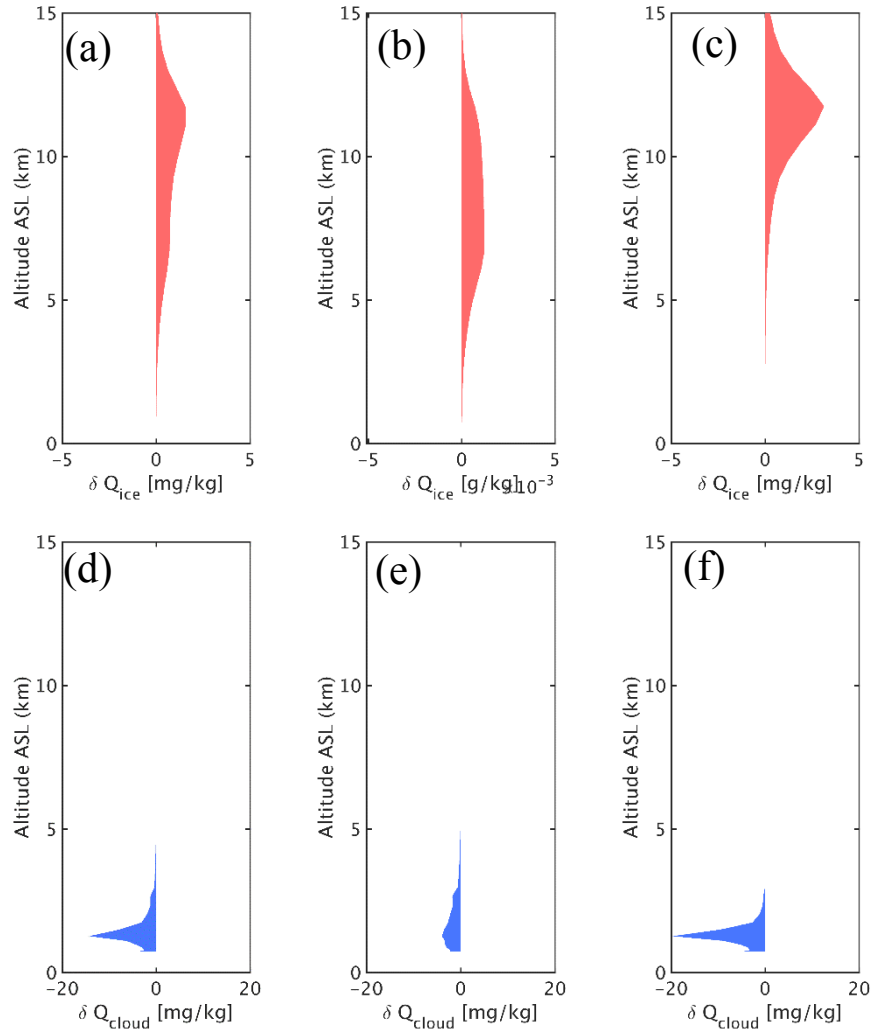
Figure 9: Vertical profile of the modification of cloud ice (a-c) and cloud water content (e-f) induced by dust over the entire simulation domain (left panel), over land (middle panel), and over ocean (right panel).
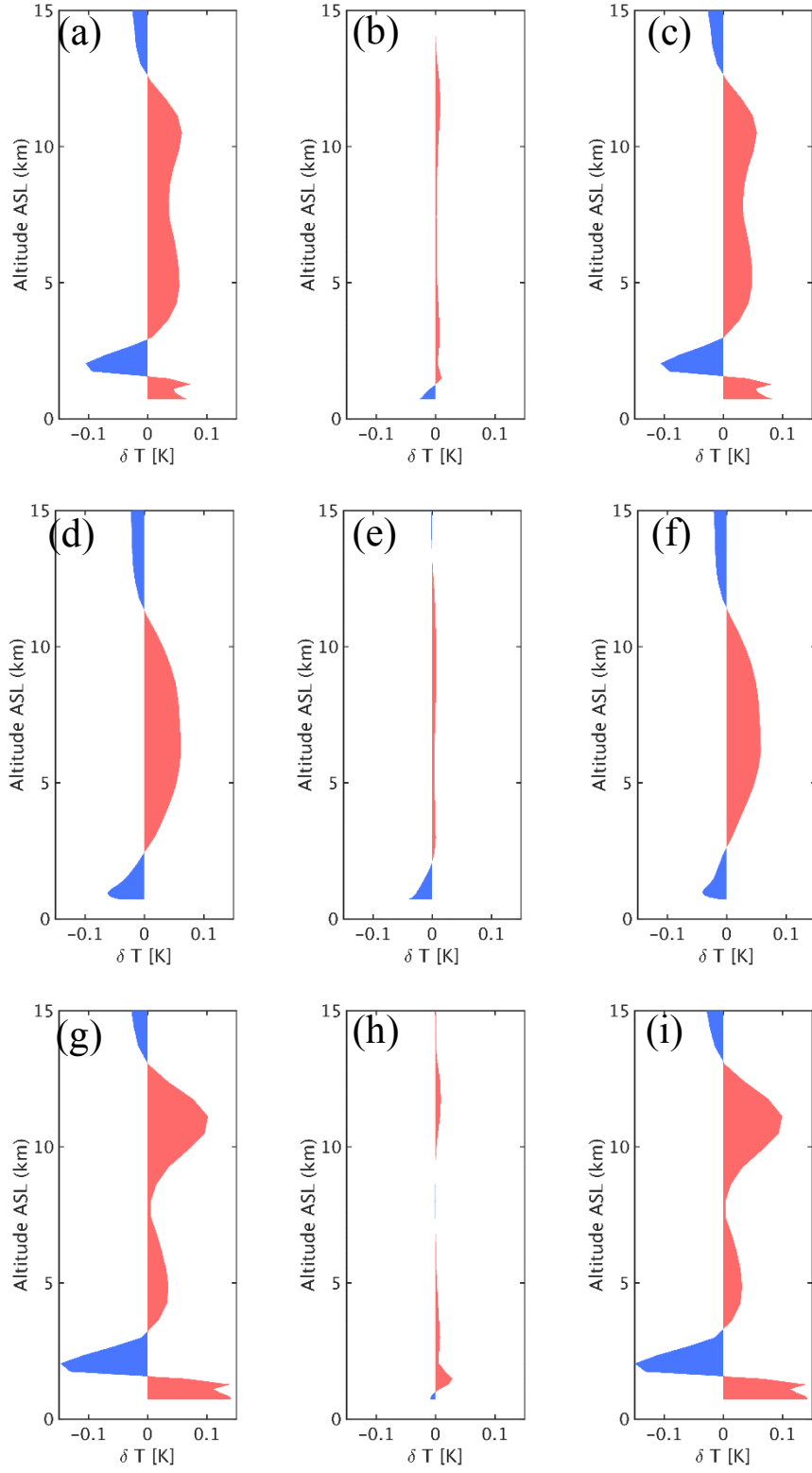
Figure 10: Modification of vertical temperature profile induced by the full effects of dust (left panel), the direct radiative effect of dust (middle panel), and the semi-direct and indirect effects of dust (right panel) over the entire simulation domain (a-c), over land (d-f), and over ocean (g-i).
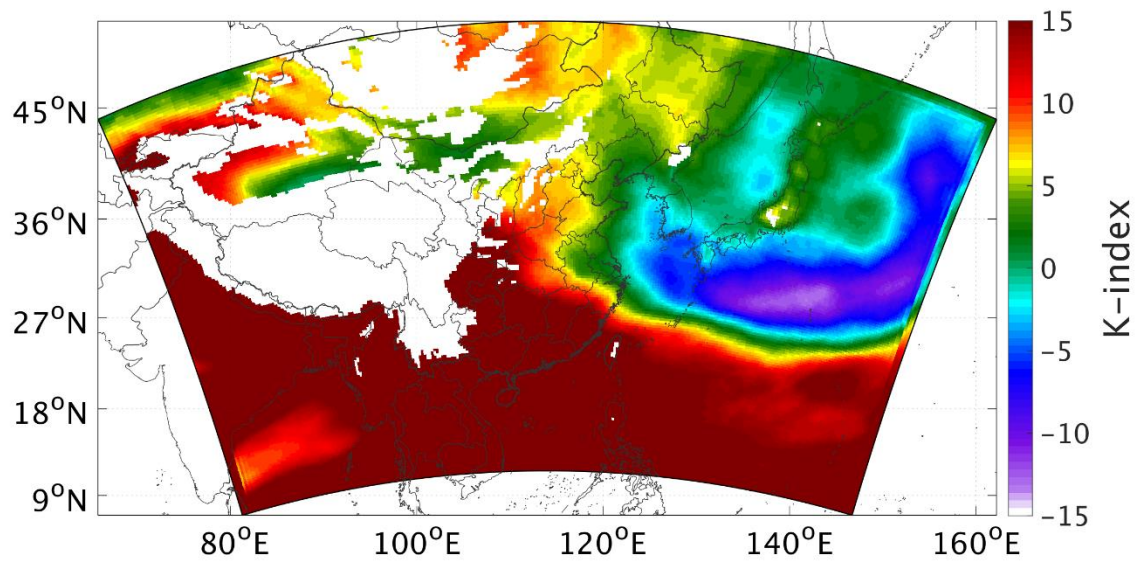
Figure 11: Spatial distributions of the monthly average K-index from NO-DUST/CLOUD.
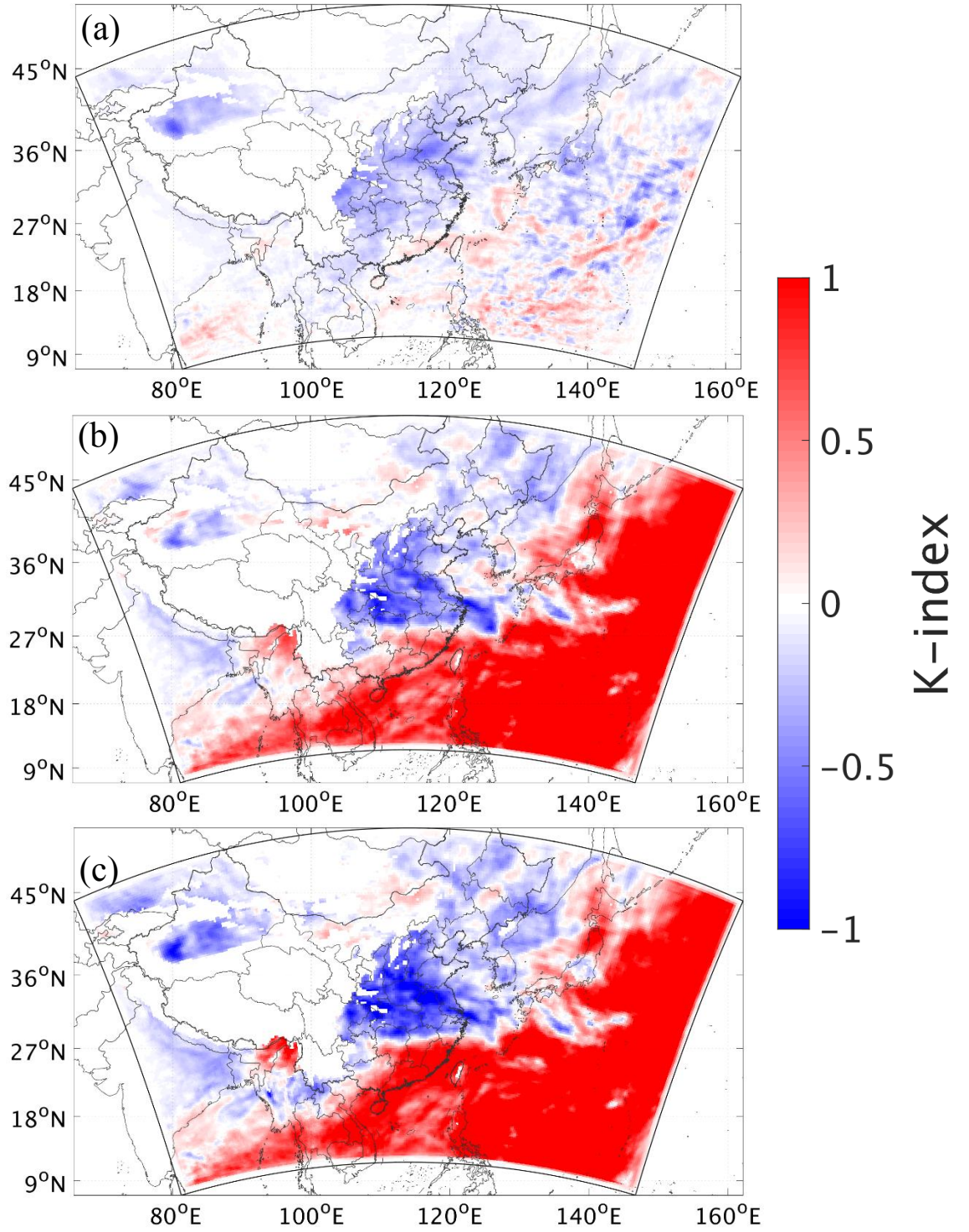
Figure 12: Spatial distributions of the modification of K-index induced by the direct radiative effect of dust (a), the semi-direct and indirect effects of dust (b), and the full effects of dust (c).
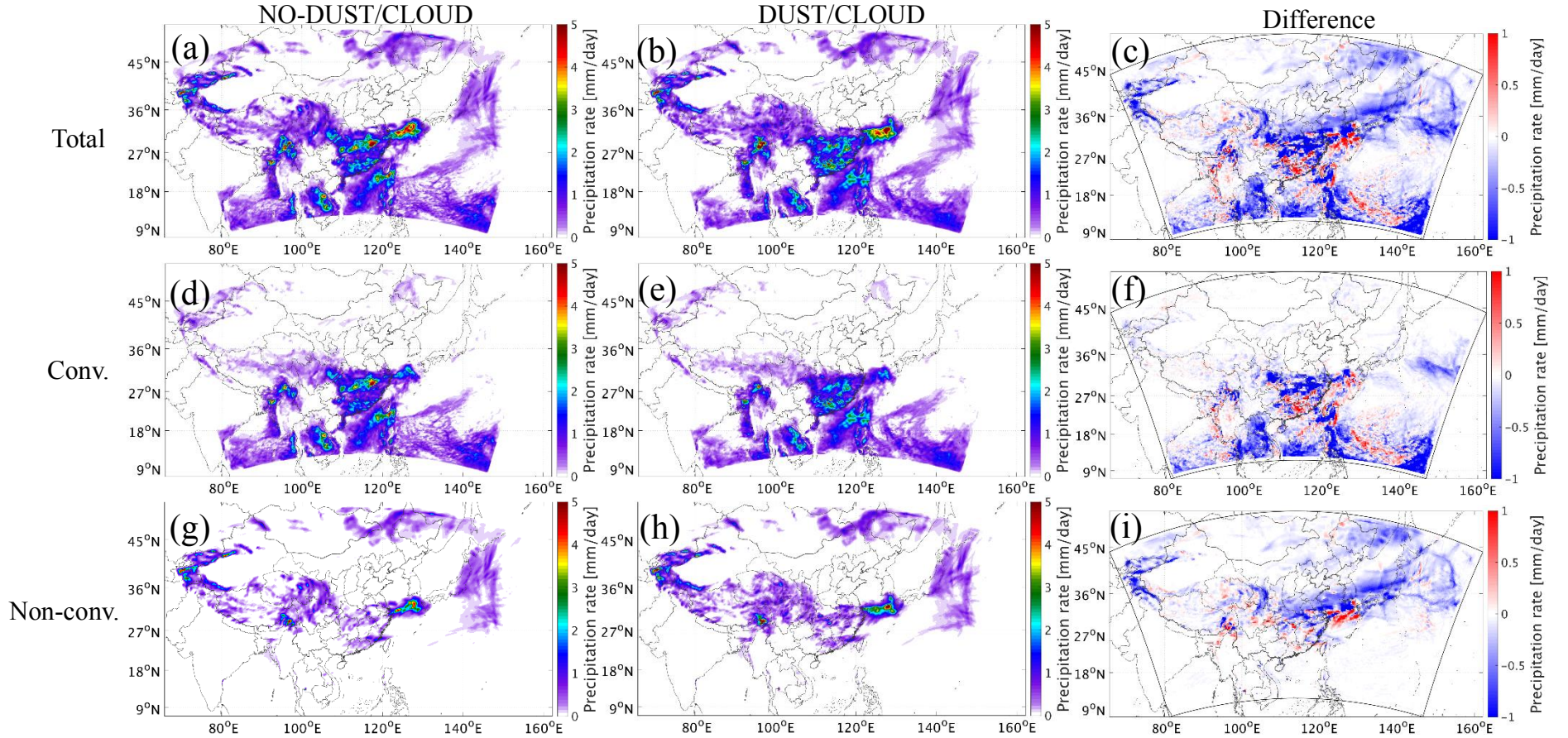
Figure 13: Spatial distributions of the average simulated total precipitation rate (a-c), convective precipitation rate (d-f), and non-convective precipitation rate (g-i) from NO-DUST/CLOUD (left panel), DUST/CLOUD (middle panel), and the difference between DUST/CLOUD and NO-DUST/CLOUD (right panel).